

© Copyright 2023

Nayana Yeshlur

Data Analysis for Detecting Intracranial Hemorrhage Using Ultrasound Tissue
Pulsatility Imaging

Nayana Yeshlur

A thesis

submitted in partial fulfillment of the
requirements for the degree of

Master of Science

University of Washington

2023

Committee:

Erika Parsons

Michael Stiber

William Erdly

Pierre Mourad

Program Authorized to Offer Degree:

School of Science, Technology, Engineering, and Mathematics

University of Washington

Abstract

Data Analysis for Detecting Intracranial Hemorrhage Using Ultrasound Tissue Pulsatility Imaging

Nayana Yeshlur

Chair of the Supervisory Committee:
Erika Parsons
School of Science, Technology, Engineering, and Mathematics

A Traumatic Brain Injury (TBI) is a type of injury that affects how the brain functions. TBI can lead to short-term problems or more long-term severe problems including various types of intracranial hemorrhage, some of which can even result in death. For this reason, finding ways of detecting intracranial hemorrhages early in patients can help to provide faster, more appropriate care, potentially improving patient outcomes. While CT and MRI are more traditional methods of diagnosing intracranial hemorrhage, they have certain drawbacks which ultrasound imaging can overcome. This work utilizes data collected from experiments on TBI patients using an ultrasound technique known as Tissue Pulsatility Imaging (TPI), specifically displacement data of brain and other tissues over the cardiac cycle. The aim of this research is to use such data to understand the differences between healthy brain displacement and brain displacement of TBI patients (with dangerous bleeding in their brain). In addition, we explore if and how the identification of the points of maximum and minimum displacement can be used to further aid in the identification of intracranial hemorrhage. The identification of these displacement points has emerged as a significant objective in this study, as they hold the potential to uncover crucial distinctions between states of wellness and illness. Furthermore, their utility in future research lies in assessing the consistency of these discoveries when applied to a broader dataset.

TABLE OF CONTENTS

List of Figures	iii
List of Tables	vii
Chapter 1. Introduction	1
1.1 Background	1
1.2 Problem Statement and Scope	3
1.3 Thesis Structure	3
Chapter 2. Related Works	4
2.1 Diagnosis of Traumatic Brain Injury	4
2.2 Diagnostic Image Segmentation	5
2.3 Tissue Pulsatility Imaging	8
2.4 UWB CSS Contribution	13
Chapter 3. Methods	17
3.1 Data Collection	17
3.2 Ultrasound Signal Processing	19
3.3 Components of Data	21
3.4 Data Processing	22
3.4.1 Averaging Displacement Data	23
3.4.2 Quadrant Displacement Data	23
3.4.3 Representative Displacement	24

Chapter 4. Results	28
4.1 Noise in Data.....	28
4.2 Data Processing Pipeline.....	29
4.3 Maximum Displacement Analysis.....	31
4.4 Principal Component Analysis	33
4.4.1 Only TBI Loading Vectors and Scree Plots.....	35
4.4.2 Only Healthy Loading Vectors and Scree Plots	39
4.4.3 Weakest Loading Vectors	44
4.4.4 Healthy vs TBI PCA Scatter Plots With Strongest Clustering	44
4.4.5 Healthy vs TBI PCA Scatter Plots With Weakest Principal Components.....	46
4.4.6 Healthy vs IPH PCA Scatter Plots With Strongest Clustering	46
4.4.7 IPH vs non-IPH PCA Scatter Plots.....	47
4.5 Experimenting With Support Vector Machine	48
Chapter 5. Conclusion and Future Work	50
Bibliography	52

LIST OF FIGURES

Figure 1.1 a. ultrasound B-mode image b. CT image c. brain and skull mask created by overlaying the ultrasound plane on the CT scan [8]	2
Figure 1.2 On the left is another example of an ultrasound B-mode image. In the middle is the processed Tissue Pulsatility displacement image. On the right is the skull mask created as described above in figure 1 [8].	3
Figure 2.1 ICHNet architecture [11].....	6
Figure 2.2 ICHNet segmentation result. Hemorrhages in red and normal brain tissue in green. (a)(b) 2D CT scan slices (left) and segmentation results (right). (c)(d) 3D ground truth masks (left) and segmentation results (right) [11].	6
Figure 2.3 U-net architecture. Next to each layer is the image dimension and on top of each layer is the number of channels or features [12]......	7
Figure 2.4 MRIAP segmentation (left) and CNN-generated segmentation (right). The tissue classes are color coded as green (WM), blue (GM), yellow (CSF), and T2 lesions (red) [12].	8
Figure 2.5 This figure shows a distribution curve of velocity displacement as a function of time during 6 cardiac cycles. The solid curve corresponds to the median, the dashed red and blue curve correspond to the first and the third quartiles [13]......	9
Figure 2.6 Hardware setup for presenting visual stimulation and collecting ECG and ultrasound data [4].	10
Figure 2.7 (a) 8 second displacement waveform during a control (non-checkerboard) visual stimulation block. (b) Modified 31 sample Hann window to taper displacement waveform. (c) One cardiac cycle before and after tapering [4].	11
Figure 2.8 (a) Displacement waveforms for four successive blocks. (b) Mean waveforms from all of the cardiac cycles for the control blocks and the checkerboard blocks [4].	11
Figure 2.9 Hardware setup for collecting ECG, End-Tidal CO ₂ , and ultrasound data [7].	12
Figure 2.10 (a) Displacement waveform from one data set from a single sample volume. (b) Displacement waveform after filtering. (c) Mean displacement waveform calculated by averaging cardiac cycles [7]......	13

Figure 2.11 (a) End-tidal CO₂ and pulse amplitude measurements from a single sample volume.
(b) Pulse amplitude versus end-tidal CO₂ from the same sample volume and best-fit line [7].
..... 13

Figure 2.12 Column one is the standardized displacement data. Column two is the ground truth CT
blood mask. Column three is the Cascade A model’s output for intracranial hemorrhage
detection [8]. 14

Figure 2.13 Loss curve for intracranial hemorrhage detection over 100 epochs [8]. 15

Figure 2.14 Dice score for intracranial hemorrhage detection over 100 epochs [8]. 15

Figure 3.1 Image shows placement of transducer at temporal window and axial, coronal, and
oblique scan angles [8]. 18

Figure 3.2 Subdural Hematoma (SDH) and Epidural Hematoma (EDH) [17]. 18

Figure 3.3 Different kinds of hemorrhage including Intraparenchymal Hemorrhage (IPH),
Intraventricular Hemorrhage (IVH), and Subarachnoid Hemorrhage (SAH) [21]... 19

Figure 3.4 Signal processing steps after collecting raw ultrasound data [22]. 21

Figure 3.5 Averaged displacement waveform over a cardiac cycle for subject DoD126. 23

Figure 3.6 Averaged displacement waveform of the four quadrants for subject DoD001. 24

Figure 3.7 Greedy algorithm for calculating representative displacement [22]. 25

Figure 3.8 Representative displacement waveform for patient DoD001 for the first right cranial
scan. 26

Figure 3.9 Patient DoD001 right coronal B-Mode scan (top left), CT scan (top middle), brain,
skull, and blood masks (top right), heart rate (bottom left), representative displacement
waveform (bottom middle), common mode motion (bottom right) [22]. 26

Figure 3.10 Representative displacement waveform for patient DoD0045 for the third left axial
scan. 26

Figure 3.11 Patient DoD045 left axial B-Mode scan (top left), CT scan (top middle), brain, skull,
and blood masks (top right), heart rate (bottom left), representative displacement waveform
(bottom middle), common mode motion (bottom right) [22]. 27

Figure 4.1 Patient DoD001 left axial B-Mode scan (top left), CT scan (top middle), brain, skull,
and blood masks (top right), heart rate (bottom left), representative displacement waveform
(bottom middle), common mode motion (bottom right). 29

Figure 4.2 On the left is the representative displacement waveform for TBI patient DoD040 for the first left axial scan. In the middle is the waveform for patient DoD040 for the second left axial scan. The full waveforms are on the top and the condensed single cardiac cycle waveforms are on the bottom. On the right is the averaged single cardiac cycle for all left axial scans for DoD040. Error bars show the standard deviation of averaged displacement frames..... 30

Figure 4.3 On the left is the representative displacement waveform for TBI patient DoD301 for the left axial scan. In the middle is the waveform for patient DoD311 for the left axial scan. The full waveforms are on the top and the condensed single cardiac cycle waveforms are on the bottom. On the right is the averaged single cardiac cycle for all healthy patients for the left axial scan angle. Error bars show the standard deviation of averaged displacement frames. 30

Figure 4.4 Condensed and averaged representative displacement data for all healthy patients at the four different scan angles. Error bars show the standard deviation of the averaged individual healthy data. 31

Figure 4.5 Occurrence rate of maximum displacement frame in healthy data. 32

Figure 4.6 Occurrence rate of maximum displacement frame in healthy data. 32

Figure 4.7 Components of Singular Value Decomposition (SVD) [24]..... 34

Figure 4.8 Right coronal only TBI, Scree Plot and Cumulative Scree Plot..... 35

Figure 4.9 Right coronal only TBI, first four loading vectors 36

Figure 4.10 Right axial only TBI, Scree Plot and Cumulative Scree Plot..... 36

Figure 4.11 Right axial only TBI, first four loading vectors 37

Figure 4.12 Left coronal only TBI, Scree Plot and Cumulative Scree Plot..... 37

Figure 4.13 Left coronal only TBI, first four loading vectors 38

Figure 4.14 Left axial only TBI, Scree Plot and Cumulative Scree Plot 38

Figure 4.15 Left axial only TBI, first four loading vectors 39

Figure 4.16 Right coronal only healthy, Scree Plot and Cumulative Scree Plot 39

Figure 4.17 Right coronal only healthy, first four loading vectors..... 40

Figure 4.18 Right axial only healthy, Scree Plot and Cumulative Scree Plot 40

Figure 4.19 Right axial only healthy, first four loading vectors..... 41

Figure 4.20 Left coronal only healthy, Scree Plot and Cumulative Scree Plot	41
Figure 4.21 Left coronal only healthy, first four loading vectors	42
Figure 4.22 Left axial only healthy, Scree Plot and Cumulative Scree Plot.....	42
Figure 4.23 Left axial only healthy, first four loading vectors	43
Figure 4.24 Weakest loading vectors for TBI data.	44
Figure 4.25 Healthy and TBI Right Coronal	45
Figure 4.26 Healthy and TBI Left Axial.....	45
Figure 4.27 Healthy and TBI Right Coronal	45
Figure 4.28 Healthy and TBI Left Axial.....	45
Figure 4.29 Healthy and TBI Left Axial.....	45
Figure 4.30 Healthy and TBI RA.....	46
Figure 4.31 Healthy and TBI LC	46
Figure 4.32 Healthy and IPH Right Axial	47
Figure 4.33 Healthy and IPH Left Axial.....	47
Figure 4.34 IPH and non-IPH Left Axial.....	48
Figure 4.35 IPH and non-IPH Right Axial	48
Figure 4.36 IPH and non-IPH Left Coronal.....	48
Figure 4.37 IPH and non-IPH Right Coronal	48

LIST OF TABLES

Table 3.1. Tissue Pulsatility Imaging variables.....	21
Table 4.2. The average maximum displacement frame and standard deviation for healthy and TBI data for every scan angle.....	32
Table 4.3. Results of T-Tests comparing frames of maximum displacement for TBI and healthy data.....	33
Table 4.4. Results of Support Vector Machine for healthy and Intraparenchymal Hemorrhage TBI data.....	49

ACKNOWLEDGEMENTS

I want to first acknowledge and thank Dr. Erdly and Dr. Stiber for acting as supervisory committee members and for providing their expertise and feedback throughout this thesis work. I next want to acknowledge Dr. Mourad who has given me so much guidance and support. Finally, I want to thank Dr. Erika Parsons for acting as my advisor and for all of her support and mentorship.

Chapter 1. INTRODUCTION

1.1 BACKGROUND

A Traumatic brain injury (TBI) is an injury that affects how the brain works [1]. There are different severities of TBI with different symptoms ranging from mild headaches to severe intracranial hemorrhaging. TBI can be fatal or result in long term complications if left undetected and untreated [2]. There were over 64,000 TBI-related deaths in the United States in 2020 [3]. Therefore, finding more efficient – yet accurate – ways of identifying TBI is a challenging and important problem. Over the past two years, a group of University of Washington¹ (UW) collaborators from Engineering, Statistics and Neurosurgery teamed up in an effort to identify intracranial hemorrhage in patients suffering from traumatic brain injuries using ultrasound.

Traditional diagnostic methods for TBI are Magnetic Resonance Imaging (MRI) and Computed Tomography (CT). Compared to CT and MRI, ultrasound is fast, portable, inexpensive, and accessible in a broader range of environments [4]. This project aims to instead use ultrasound to detect intracranial hemorrhaging. Ultrasound works by propagating sound waves through tissue using a transducer. That sound can either be reflected, scattered, refracted, or absorbed. The sound that is echoed back to the transducer informs an image of structure or velocity. Brightness Mode or B-Mode imaging uses the amplitude of the echoed sound to plot a two-dimensional image of tissue structure. Doppler ultrasound uses the frequency of the echoed sound to determine tissue or blood velocity [5].

Terason Incorporated's ultrasound device is portable and more cost efficient than alternative imaging technologies and can therefore be used in less accessible environments such as a combat setting [6]. However, ultrasound has its own weaknesses when applied to the identification of intracranial hemorrhage. In particular the adult skull poses a problem as ultrasound cannot penetrate effectively. This prevents the creation of sufficiently useful B-mode images. Researchers at UW have been utilizing a technique called Tissue Pulsatility Imaging (TPI) to overcome the weaknesses of ultrasound. TPI adapts tissue Doppler signal processing methods

¹ Project initially sponsored by the Department of Defense and worked in collaboration with Terason Portable Ultrasound

to measure tissue displacement or strain due to blood flow over the cardiac and respiratory cycles [7]. During systole blood accumulates in vessels in tissue and causes the tissue to expand, and during diastole blood flows out of vessels in the tissue and back toward the heart causing the tissue to relax. TPI measures local changes in tissue blood volume between the period of expansion and relaxation [7].

Over the past few years data has been collected from civilian patients at Harborview Medical Center suffering from moderate to severe TBI. Initial CT scans were taken to diagnose the patients with TBI and intracranial hemorrhaging. Follow-up ultrasound scans of the same patients were collected to provide input data for this project. Ultrasound scans were taken in the same locations of the head as the CT scans. The collected ultrasound data was processed into TPI data by the UW team, and the collected CT data had been used as ground truth for comparison. Figure 1.1 shows an ultrasound B-mode image, a CT scan image, and the overlay of the ultrasound plane and CT scan to create different masks. Figure 1.2 shows an ultrasound B-mode image, an image of displacement, and the mask showing the presence of skull.

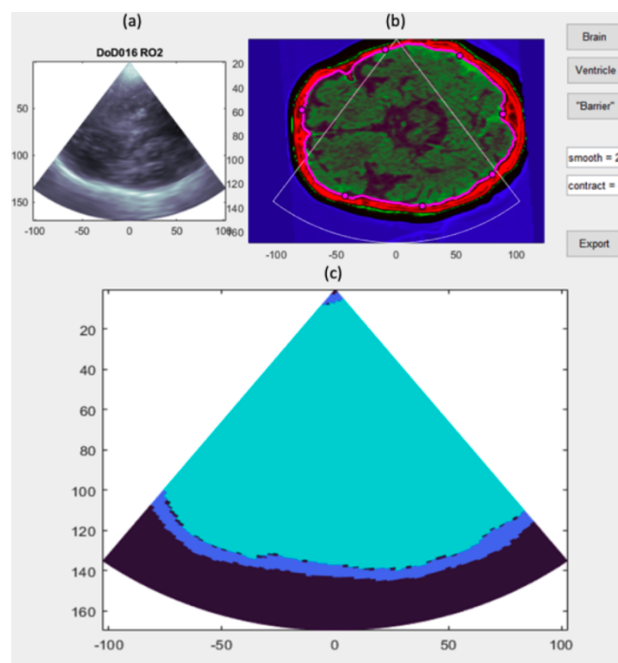


Figure 1.1 a. ultrasound B-mode image b. CT image c. brain and skull mask created by overlaying the ultrasound plane on the CT scan [8]

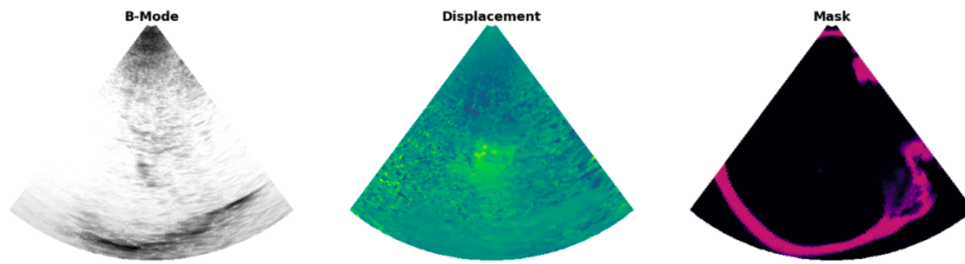


Figure 1.2 On the left is another example of an ultrasound B-mode image. In the middle is the processed Tissue Pulsatility displacement image. On the right is the skull mask created as described above in figure 1 [8].

1.2 PROBLEM STATEMENT AND SCOPE

The aim of this research is to better understand and utilize TPI data. The primary goal is to develop a representation of displacement in the brain caused by the cardiac cycle. Based on this representation the displacement data for TBI and healthy subjects will be compared. Features contained in displacement data that could potentially aid in the detection of intracranial hemorrhage are to be identified.

The goals of this research will allow for better understanding of the application of ultrasound to TBI and intracranial hemorrhage detection. If ultrasound can differentiate TBI patients and identify intracranial hemorrhage, this could improve the efforts of treatment and improve patient outcome, especially in applications outside of traditional diagnosis methods.

1.3 THESIS STRUCTURE

Chapter 2 will discuss related works including those that study the diagnosis of traumatic brain injury, diagnostic image segmentation, tissue pulsatility imaging, and the contributions from UWB CSS students. Chapter 3 will discuss how the data was collected, how it was processed, and system setup. Chapter 4 will discuss the results of this thesis. Chapter 5 will discuss the conclusion of work and potential future work.

Chapter 2. RELATED WORKS

2.1 DIAGNOSIS OF TRAUMATIC BRAIN INJURY

There has been a lot of prior research into diagnosing traumatic brain injury through imaging and other methods. One study looked at diagnosing the severity of cerebral edemas in pediatric traumatic brain injury cases [9]. Pediatric brains, brains of patients typically under the age of 18, are more prone to developing cerebral edemas after TBI, than adults. This can mean an increased likelihood of secondary issues caused by the cerebral edema and a smaller window in which to diagnose and treat pediatric TBI patients. One of the main goals of this study was to design an automated densitometry analysis of CT images to classify the severity of cerebral edemas. When looking at CT imaging the density of a material is defined as its ability to absorb X-ray photons, this is measured in Hounsfield Units (HU). Using the Marshall classification, patients were grouped as mild or severe edema patients, with some patients having delayed severe edema. Using HU values, major intracranial components (Cerebrospinal Fluid (CSF), normal cerebral tissue, and blood) were classified and then a threshold was set so that nothing else in the head (cranium) was included in the analysis. The overall CT image density of severe edema patients was much higher than in mild edema patients. The proportion of pixels with $HU = 17$ to 24 was highly correlated with severe cerebral edema with a p -value $< .01$. This proportion was also able to differentiate patients who developed delayed cerebral edema from those who were mild TBI patients [9].

Another study looked at whether CT and MRI data could help to predict the 3-month outcome in mild traumatic brain injury (MTBI) [10]. This is to better understand the persistent impairment that can result from MTBI, so that more effective treatment can be implemented. It is widely accepted that certain clinical, demographic, and socioeconomic factors such as age, previous head injury, education, and employment status can contribute to poorer outcomes from MTBI. The study assessed the clinical relevance of early CT and MRI to 3-month outcomes after controlling for those factors. Patients were brought into the ER and evaluated for acute head injury. A CT scan was done upon admission to the ER and an MRI scan was done on average 12 days after admission. The measure of outcome used was the 8-point Extended Glasgow Outcome Scale (GOS-E), which is an assessment of global function. Demographic, socioeconomic, and imaging

data were assessed to predict GOS-E 3 months after injury. Twenty-seven percent of patients with normal CT scans when admitted had abnormal MRI scans later. Evidence of subarachnoid hemorrhage in CT scans was associated with a poorer 3-month outcome, after adjusting for demographic, clinical, and socioeconomic factors. One or more brain contusions on MRI and > 4 foci of hemorrhagic axonal injury on MRI, were associated with a poorer 3-month outcome, after adjusting for CT findings, demographic, clinical, and socioeconomic factors. Taking the demographic features in addition to the CT and MRI data resulted in more than a 2-fold increase in the explained variance of GOS-E after 3 months [10].

2.2 DIAGNOSTIC IMAGE SEGMENTATION

There has been prior research into segmenting medical images for diagnostic purposes. This includes images derived from CT, MRI, and ultrasound. One study proposes the use of a multi-task full convolutional network ICHNet to detect, classify, and segment intracranial hemorrhage (ICH) using 3D CT scans [11]. ICH can be categorized into five subtypes based on the bleeding location, and combination of bleeding location and ICH volume are factors associated with mortality and treatment outcome. Most previous work has treated ICH detection and segmentation as two independent tasks. This research proposes a unified fully convolutional network for ICH classification and segmentation simultaneously, referred to as ICHNet. The aim of the segmentation task is to classify each pixel in the CT image as: hemorrhage, normal brain tissue, and non-brain (skull and outside the skull). The classification tasks are a binary ICH detection task and a subtype classification task, for each slice and for the whole scan. ICHNet contains a shared encoder to extract features for both classification and segmentation tasks while utilizing a convolutional long short-term memory (ConvLSTM) module to capture sequential information embedded in consecutive slices. ICHNet generally outperforms the chosen baseline models (3D/2D ResNet18 for classification and 3D U-Net for segmentation) as well as ICHNet models that only either perform the segmentation task or classification task (ICHNet_{cls} and ICHNet_{seg}) across all metrics. [11]

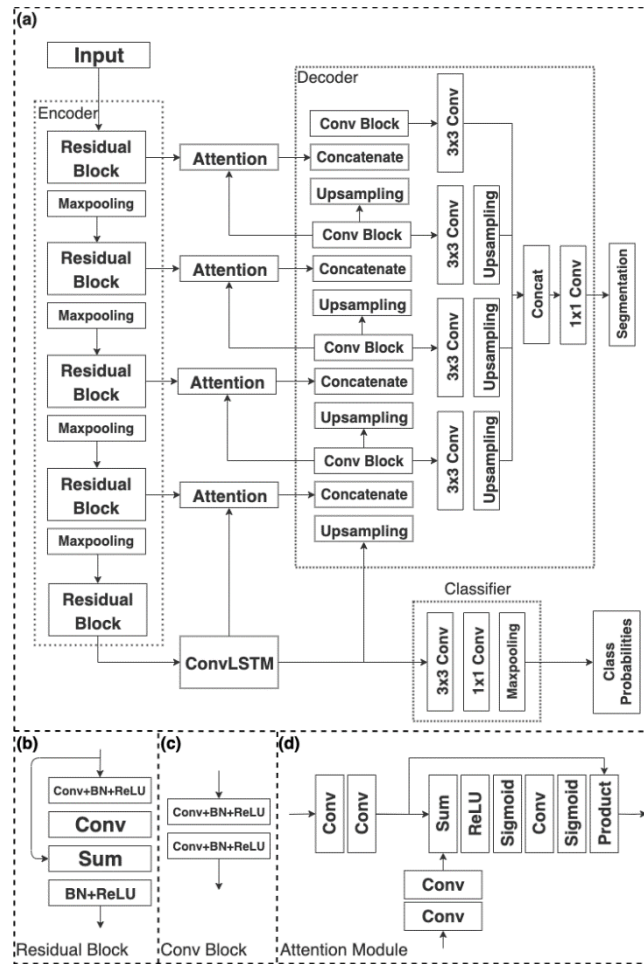


Figure 2.1 ICHNet architecture [11]

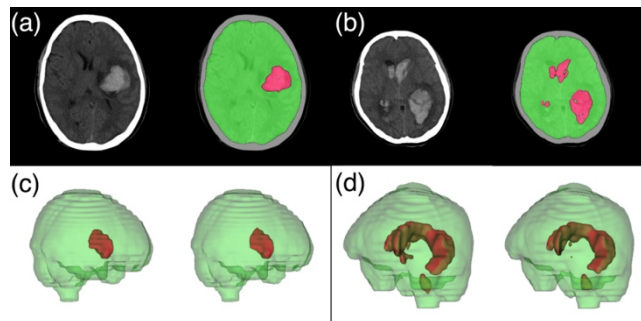


Figure 2.2 ICHNet segmentation result. Hemorrhages in red and normal brain tissue in green. (a)(b) 2D CT scan slices (left) and segmentation results (right). (c)(d) 3D ground truth masks (left) and segmentation results (right) [11].

Another study utilized multi-channel MRI scans and deep convolutional neural networks (CNNs) for brain tissue classification of Multiple Sclerosis (MS) patients [12]. MS is a neurological disease that affects the central nervous system (CNS) and is characterized by the presence of sclerosis or lesions in the CNS. Volumetric measures of tissues, specifically lesions, on MRI has been used for diagnosis and treatment management. The dataset came from the CombiRx database which is a multi-center, double-blinded, and randomized phase III clinical trial for MS. 500 images were randomly sampled from the CombiRx database. Pre-processing of the image dataset before input into the models included alignment of all images into the T2-weighted image space using rigid-body registration, removing non-brain tissue (skull stripping) using a brain extraction tool (BET), bias field correction to reduce the effects of intensity inhomogeneity, intensity normalization, and de-noising using adaptive anisotropic diffusion filtering. A multi-class U-net CNN is used for segmenting brain tissue into white matter, grey matter, CSF, and T2-hyperintense white matter lesions (T2 lesions). Ground truth segmentation was obtained using Magnetic Resonance Imaging Automated Processing (MRIAP), a validated software package, which was further validated by experts as a part of the CombiRx trial. The Dice Similarity Coefficient (DSC) was calculated for the class-specific accuracy. Quantitative assessment showed high similarity between the output of the U-net model and the validated MRIAP segmentation in the test set, with DSC values of 0.94 for white matter and grey matter, 0.97 for cerebrospinal fluid, and 0.85 for T2 hyperintense lesions [12].

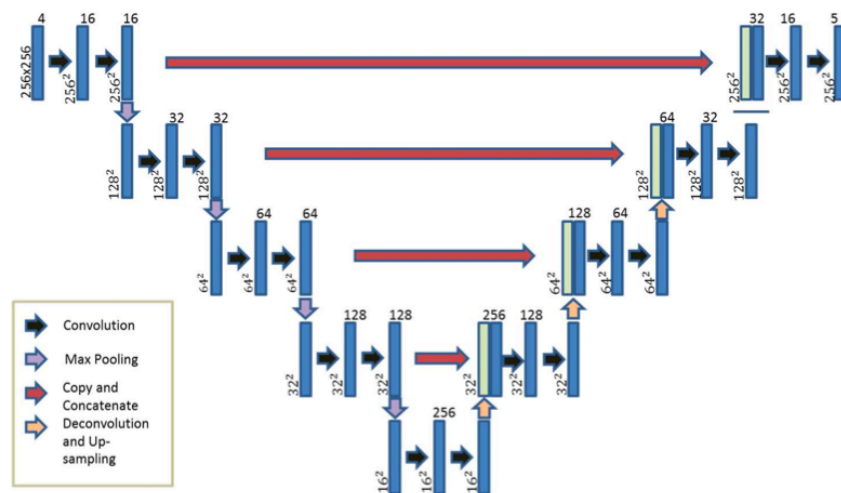


Figure 2.3 U-net architecture. Next to each layer is the image dimension and on top of each layer is the number of channels or features [12].

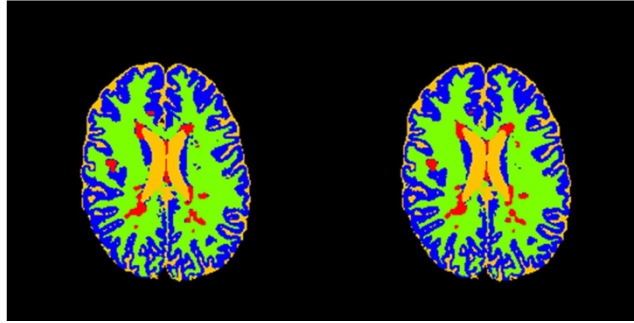


Figure 2.4 MRIAP segmentation (left) and CNN-generated segmentation (right). The tissue classes are color coded as green (WM), blue (GM), yellow (CSF), and T2 lesions (red) [12].

2.3 TISSUE PULSATILITY IMAGING

Tissue Pulsatility Imaging (TPI) has been utilized outside of the TBI project at UW. One study looked at the relationship between Leukoaraiosis (LA), lesions of the white matter, and brain tissue velocity due to pulsed cerebral perfusion, using TPI [13]. LA may be an indicator for decreased prognosis of stroke and myocardial infarction in patients and cerebral hypo-perfusion may be linked to LA. In addition to TPI, MRI examinations were also performed to obtain a volumetric analysis. The aim being to compare the brain tissue motion as assessed by TPI with LA volume as assessed by MRI. Because brain microvascular damage with LA is more frequent and rapidly evolving among women than men of the same age, only female subjects were sampled. Thirteen women fit the inclusion criteria and were included in this study. Out of thirteen participants to the study three were excluded due to intracranial abnormalities found on MRI and bad quality acquisition of TPI.

Transcranial ultrasound acquisitions were performed with a 2 MHz phased array probe through the right transtemporal bone window. For each subject, 179 images are acquired with a sampling frequency of 40 MHz and a frame rate of 30 frames per second, resulting in 6 seconds of acquisition. We then obtained a transverse scan of the brain every 33 milliseconds, and each frame contains 112 Radio Frequency scan lines. Tissue Pulsatility of the brain was estimated using 1D- intercorrelation methods. Velocity displacement was measured along the ultrasound beam axis and band-pass filtered to eliminate the effect of respiratory cycles. The result was a 3D velocity displacement matrix with the two first dimensions corresponding to depth and width of the brain

image and the last dimension representing the time axis corresponding to the total number of frames [13].

The maximum velocity of displacement (TPI_{max}) was 0.89 ± 0.30 mm/s. The mean absolute volume (V_{Abs}) of LA was 7 ± 6.34 ml and the mean relative volume (V_{Rel}) of LA was 0.66 ± 0.57 %. There was a significant negative correlation between TPI_{max} and LA volume, V_{Abs} ($\rho = -0.79$, $p < 0.02$) and V_{Rel} ($\rho = -0.81$, $p < 0.01$). There is a significant negative correlation between maximum cerebral tissue pulsatility evaluated by ultrasound and TPI and the volume of LA measured by MRI. The maximal cerebral velocity displacement decreases when the volume of LA increases. This is consistent with the idea that greater LA is associated with lower cerebral perfusion [13].

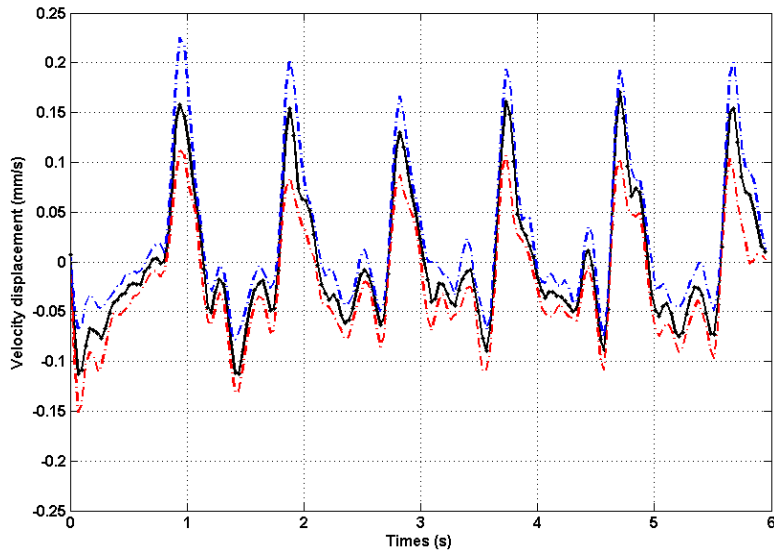


Figure 2.5 This figure shows a distribution curve of velocity displacement as a function of time during 6 cardiac cycles. The solid curve corresponds to the median, the dashed red and blue curve correspond to the first and the third quartiles [13].

Research utilizing TPI has been ongoing at UW for many years. One study looked at functional Tissue Pulsatility Imaging (fTPI) of the brain to detect activation during visual stimulation [4]. fTPI is an ultrasound technique developed to map brain function by measuring changes in tissue pulsatility due to changes in blood flow with neuronal activation. TPI is based on plethysmography, an older, non-ultrasound technology for measuring expansion of a whole-body part due to perfusion over the cardiac cycle. TPI uses tissue Doppler signal processing

methods to measure this pulsatile plethysmographic signal in an ultrasound image plane. Though the mechanisms are not fully understood, it is generally accepted that neural activation triggers vasodilation which means increased blood flow to activated areas in the brain. Two subjects participated in the study. A contrast-reversing checkerboard block paradigm was used to stimulate the visual cortex, alternating control, and checkerboard blocks. Triggering of the visual stimuli was synchronized with the triggering of ultrasound and Electrocardiogram (ECG) data acquisition.

Ultrasound data was collected trans-cranially from the occipital lobe. A total of 240 frames of radio frequency ultrasound were recorded at 30 frames per second. Data collection was started 10 seconds into each block to allow sufficient time for the blood flow to change in response to the neuronal stimulation. Tissue displacement was measured using the 2D autocorrelation estimator, which additionally estimates the mean change in phase of the signal to calculate the local ultrasound center frequency and uses the wavelength at that frequency to derive velocity or displacement. The amplitude of the displacement waveforms of the mean checkerboard waveform is larger than the amplitude of the mean control waveform as would be expected if blood flow and tissue pulsatility increases during visual stimulation. Large regions of statistically significant activation during visual stimulation were detected in 4 of 7 studies for the male subject and in 3 of 7 studies for the female subject. The active regions appear to correlate with the paths of vessels that supply the visual cortex [4].

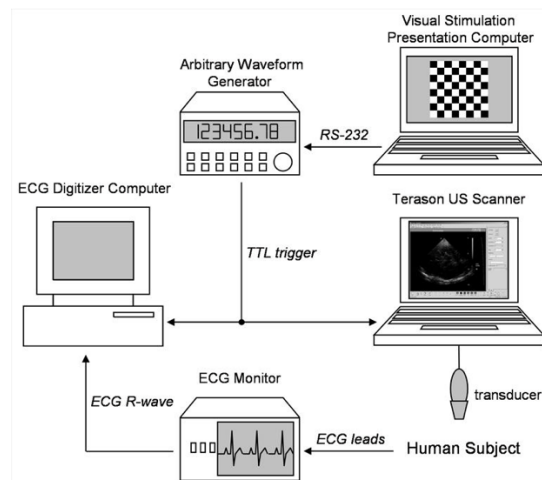


Figure 2.6 Hardware setup for presenting visual stimulation and collecting ECG and ultrasound data [4].

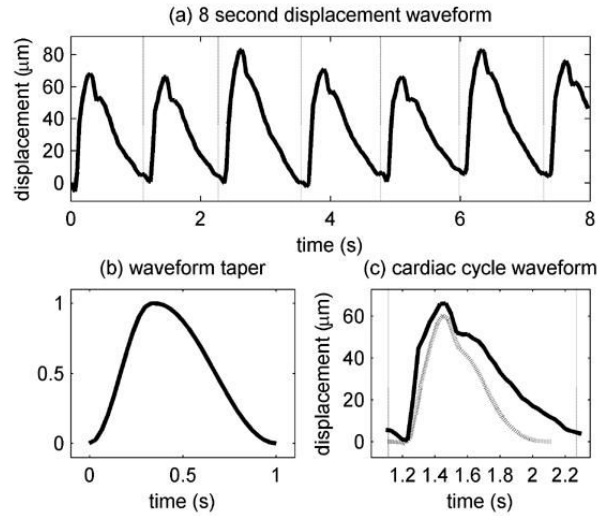


Figure 2.7 8 second displacement waveform during a control (non-checkerboard) visual stimulation block. (b) Modified 31 sample Hann window to taper displacement waveform. (c) One cardiac cycle before and after tapering [4].

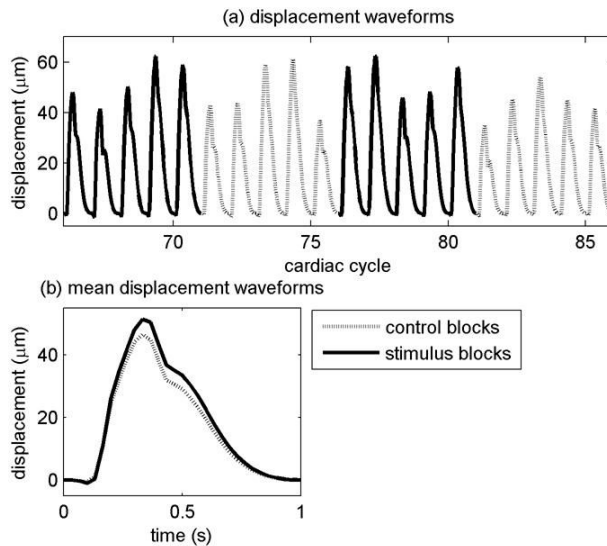


Figure 2.8 (a) Displacement waveforms for four successive blocks. (b) Mean waveforms from all of the cardiac cycles for the control blocks and the checkerboard blocks [4].

Another study looked at TPI of cerebral vasoreactivity during hyperventilation [7]. Cerebral vasoreactivity (CVR) is the ability of the cerebral arterioles to respond to changes in arterial CO₂ partial pressure (PaCO₂) in order to regulate blood flow and oxygen delivery to the brain. Under normal conditions an increase in PaCO₂, will cause the cerebral arterioles to dilate

reducing vascular resistance and increasing cerebral blood flow (CBF). A decrease in arterial PaCO₂, will cause the cerebral arterioles to constrict increasing vascular resistance and reducing CBF. Measurement of CVR has been used to evaluate cerebral vascular function over a broad range of clinical applications. Tissue pulsatility was measured in four subjects through the temporal acoustic window before, during, and after voluntary hyperventilation, and the results were correlated with the subjects' end-tidal CO₂ measurements collected concurrently. In each subject, decreases in tissue pulsatility during hyperventilation were observed that were statistically correlated with the subject's end-tidal CO₂ measurements. There were, however, regions where pulsatility increased and regions without statistically significant changes in pulsatility. The median percent change in tissue pulsatility for a change in end-tidal CO₂ from 40 mmHg to 20 mmHg ranged from 50% for the youngest subject to 25% for the oldest subject. Additional studies are needed to expand the results to a larger population and to assess the accuracy of the technique in identifying subjects with compromised CVR.

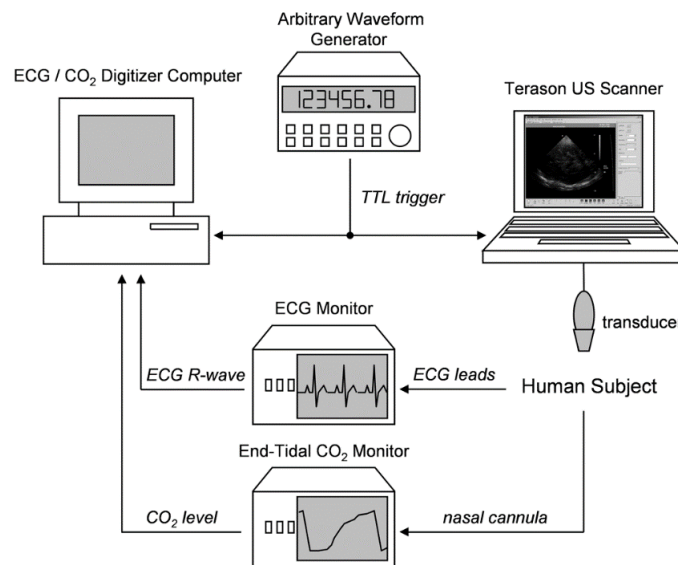


Figure 2.9 Hardware setup for collecting ECG, End-Tidal CO₂, and ultrasound data [7].

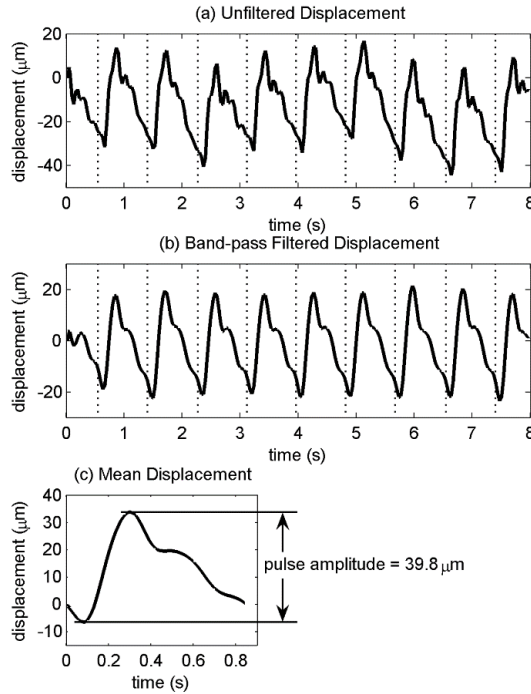


Figure 2.10 (a) Displacement waveform from one data set from a single sample volume. (b) Displacement waveform after filtering. (c) Mean displacement waveform calculated by averaging cardiac cycles [7].

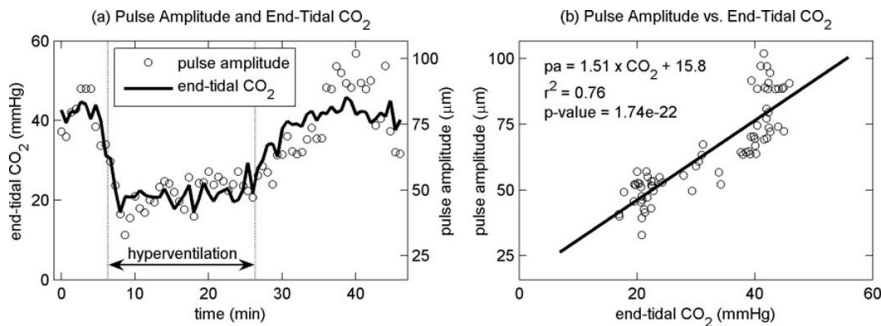


Figure 2.11 (a) End-tidal CO₂ and pulse amplitude measurements from a single sample volume. (b) Pulse amplitude versus end-tidal CO₂ from the same sample volume and best-fit line [7].

2.4 UWB CSS CONTRIBUTION

Previous work by a CSS student utilized TPI displacement data to implement deep learning models to detect skull, brain, ventricle, and blood. CT derived masks were used to label ground truth and assess the accuracy of the models [8]. UNet, UNet++, Attention UNet, and Cascade deep

learning models were utilized. U-Net is a popular and promising choice in various types of medical segmentation tasks. So, all models used in this project have U-Net as the backbone network. The dice loss function was used as the objective loss function. U-Net++ was chosen for its ability to improve the gradient flow. In image segmentation the attention mechanism is a way to highlight relevant activations during training, which allows focus on a particular part of an image. The cascade model uses a combination of a coarse model and a fine model for segmentation. The metrics used for evaluation were dice coefficient score, intersection over union (IoU) score, precision, and recall. All of the models ultimately performed poorly in detecting intracranial hemorrhage. There was greater success with skull and ventricle detection. Some of the setbacks of this project were limited data, limited diversity in data which impacts generalizability, class imbalance with blood being a small percentage of total pixels, and sub-optimal data collection protocol where ultrasound data collection was delayed [8].

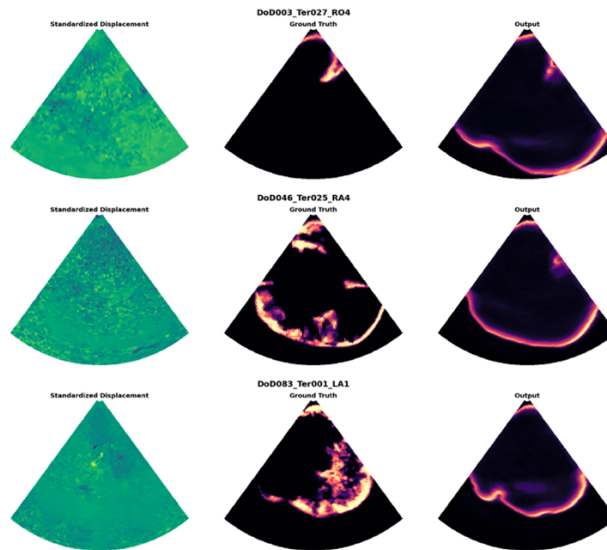


Figure 2.12 Column one is the standardized displacement data. Column two is the ground truth CT blood mask. Column three is the Cascade A model's output for intracranial hemorrhage detection [8].

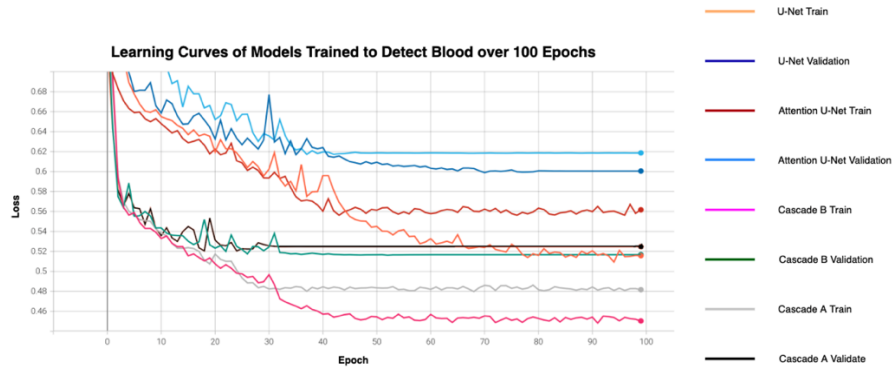


Figure 2.13 Loss curve for intracranial hemorrhage detection over 100 epochs [8].



Figure 2.14 Dice score for intracranial hemorrhage detection over 100 epochs [8].

So far, no models have been able to achieve sufficiently good performance (from a clinical perspective) when trying to detect intracranial hemorrhage. The displacement data used in the previous work was the 8th displacement frame within a given cardiac cycle. The displacement data is a time series of the degree of movement over eight seconds. The 8th frame was selected as it likely contained the point at which the blood volume is maximum in the head. Some additional later preliminary work has shown that this may not actually be the most effective frame to detect intracranial hemorrhage.

Another CSS student described how ultrasound B-Mode and TPI displacement data can be utilized to implement deep learning models to detect the skull, brain, ventricles, and blood [14]. CT derived masks were used to label ground truth and assess the accuracy of the models at detecting these structures and condition. The model used was pix2pix. Additionally, B-Mode data and Generative Adversarial Networks (GANs) such as StyleGan2-ada were used to create synthetic ultrasound data to simulate intracranial hemorrhage. This project achieved similar results

to the other project, models detecting intracranial hemorrhage had poor performance. The synthetic data seemed promising but needs further research.

Chapter 3. METHODS

3.1 DATA COLLECTION

Data for this project was collected at Harborview Medical Center in Seattle, WA. When patients arrived at Harborview, they initially received a diagnosis of traumatic brain injury via CT and if necessary, received treatment. They were then screened for inclusion in this study based on the type of injury. Ultrasound data was collected using a Terason u3200t tablet based, general-purpose scanner. This scanner has a 4V-2 phased array transducer (64 elements, 2.5 MHz RF sampling frequency, 128 scanlines per frame). The ultrasound scans were conducted sometime after injury and TBI diagnosis, ranging from hours to days later.

For the TBI patients the protocol was each subject was initially scanned about 30 times. 15 scans from the left side of the head and 15 scans from the right side. Data was collected through the temporal window of the head. Each side of the head received 5 axial scans, 5 coronal scans, and 5 oblique scans. The oblique scan angle positions were determined based on CT imaging of the injury. During scanning a pulse oximeter was also used to capture patients' heart rate. The scanning protocol changed due to Covid restrictions, with subjects later receiving fewer scans.

In addition to data collection from TBI patients, a group of healthy patients with no TBI have received scans more recently. Each healthy patient was scanned a total of 38 times. 19 on each side of the head starting at 0 degrees, incrementing by 10 degrees, and ending at 180 degrees. 0 degrees and 180 degrees were labeled as axial, and 90 degrees was labelled coronal. Any angles in between are oblique. The right side was scanned first. The left side (-xAxis) was always towards the nose at 0 degrees, and towards the top of the head at 90 degrees. See figure 3.1 for illustration of scan angles.

A total of 100 TBI subjects have had scans collected and data processed for use in this research. Subjects with poor scan quality and incorrect data format were excluded. Scan quality refers to how many artifacts, such as movement, the data and scan contain. Scan quality was determined by UW researchers and ultrasound experts. A total of 12 healthy subjects have had scans collected and data processed for use in this research. This work only utilizes the axial and coronal scans. The oblique scans were not used because the scan angles for healthy and TBI subjects were not the same across all patients and so would not be comparable.

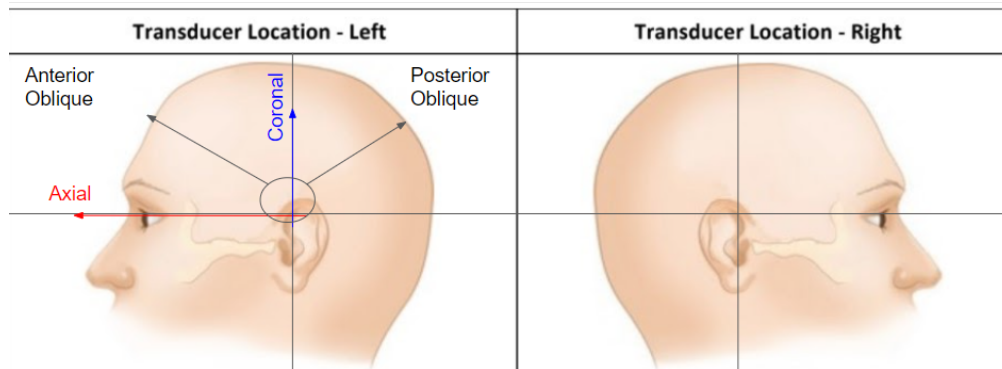


Figure 3.1 Image shows placement of transducer at temporal window and axial, coronal, and oblique scan angles [8].

The TBI subjects' injuries were categorized into 5 general types of injury: Epidural Hematoma, Subdural Hematoma, Subarachnoid Hemorrhage, Intraparenchymal Hemorrhage, and Intraventricular Hemorrhage. Many subjects were identified as having multiple types of injuries. Epidural Hematoma (EDH) occurs when blood accumulates between the skull and the dura mater. The dura matter is a thick membrane covering the brain. The injury typically occurs when a skull fracture tears an underlying blood vessel. EDH is half as common as Subdural Hematomas (SDH) [15]. SDH occurs when a clot of blood develops between the surface of the brain and the dura mater. This occurs when a head injury jolts or shakes the brain and causes stretching or tearing of veins on the brain's surface [16].

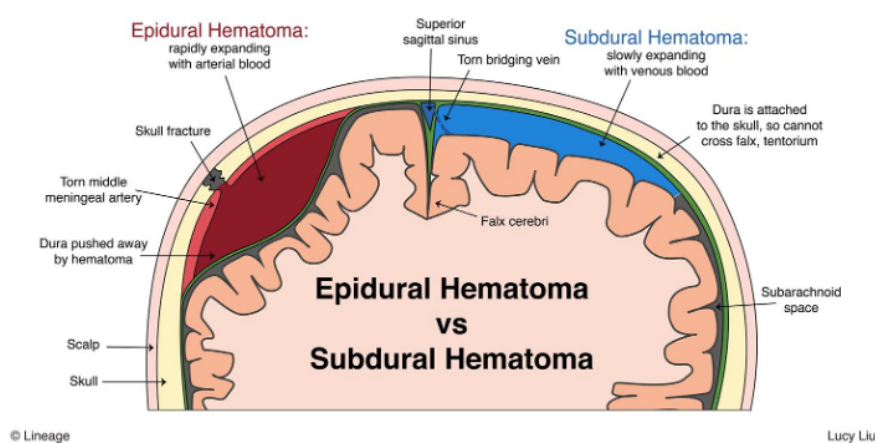


Figure 3.2 Subdural Hematoma (SDH) and Epidural Hematoma (EDH) [17].

Intraparenchymal Hemorrhage (IPH) is one type of intracerebral bleeding, the other type is Intraventricular Hemorrhage (IVH). IPH occurs when there is bleeding in the parenchyma. Parenchyma refers to the functional tissue in the brain. [18]. IVH occurs when there is bleeding inside and around the brain’s ventricular system [19]. Subarachnoid Hemorrhage (SAH) occurs when there is bleeding in the subarachnoid space, which is the area between the arachnoid membrane and the pia mater [20].

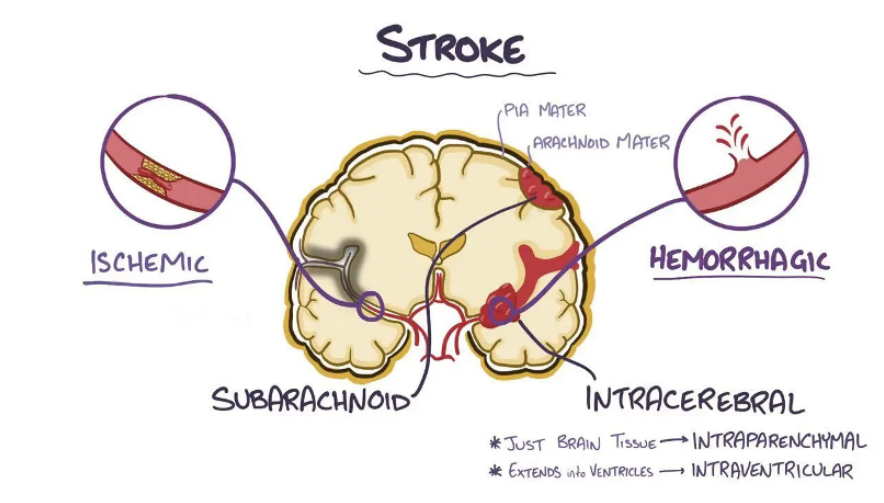


Figure 3.3 Different kinds of hemorrhage including Intraparenchymal Hemorrhage (IPH), Intraventricular Hemorrhage (IVH), and Subarachnoid Hemorrhage (SAH) [21].

3.2 ULTRASOUND SIGNAL PROCESSING

Diagnostic ultrasound transmits and receives high frequency sound typically between 1 and 10MHz. The higher the frequency the better the imaging resolution, however the depth of penetration is reduced. In this application the skull is very attenuative and so a low frequency was used at 2.5MHz [22]. Due to differences in local tissue acoustic impedance, when sound is propagated through the body only a fraction of the sound is scattered back towards the ultrasound transducer. The speed of sound in tissue is relatively constant and so a 2-dimensional image of tissue structure, called B-Mode, can be created based on the amplitude of the signal received back and the time between sound burst transmission and reception. Images of blood or tissue velocity, called Tissue Doppler, can be created by transmitting two or more bursts of ultrasound and measuring the spatially localized relative temporal shifts in the received ultrasound from burst to

burst. Tissue Pulsatility Imaging (TPI) is a variation of Tissue Doppler designed to measure the pulsatile motion of tissue due to blood flow. During systole, blood accumulates in the arterial vasculature, causing the tissue to expand. Later in the cardiac cycle, accumulated blood flows through into the venous vasculature and back towards the heart, allowing the tissue to relax to its pre-systolic blood volume [7]. It is hypothesized that TPI can be used to detect variations in tissue pulsatility localized to areas of the brain experiencing hemorrhage.

The ultrasound raw data was filtered into 8 frequency sub-bands, and then it was quadrature demodulated which filters ultrasound RF and converts it into a complex signal. The velocity for each sub-band was computed using lag 1 autocorrelation, which calculates velocity from the change in phase between successive frames. The calculated velocities were averaged and weighted by the power of the sub-band [22]. This yielded an 8 second velocity waveform for every pixel in the image sequence. Next a Vector-Doppler weighted-least squares method was applied across the entire frame to suppress common-mode motion introduced by gross motion of the ultrasound transducer relative to the patient. Tissue displacement was calculated from the time integral of velocity and combined with a band-pass filter, with cutoffs of .5Hz and 5 Hz, to emphasize cardiac pulsatility. Lastly, individual cardiac cycles within the 8 seconds were detected and resampled such that all cycles were of a uniform duration of 30 samples per cardiac cycle. Each displacement waveform for each cardiac cycle was tapered to 1 second to handle the variable durations of the cardiac cycles. A modified 31 sample Hann window was used to taper the displacement waveforms [22]. Resampling and tapering the cardiac cycle waveform can be seen in figure 2.7. Figure 3.5 outlines the signal processing steps.

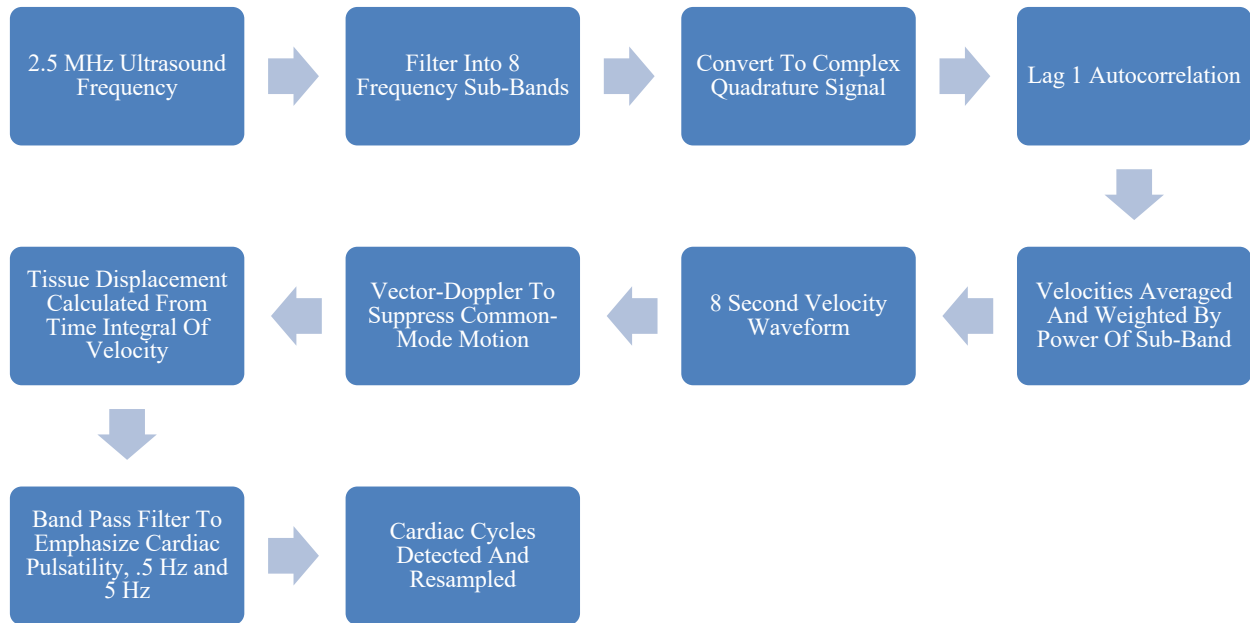


Figure 3.4 Signal processing steps after collecting raw ultrasound data [22].

3.3 COMPONENTS OF DATA

Each processed Tissue Pulsatility Imaging file used in this project contains the following variables:

Table 3.1. Tissue Pulsatility Imaging variables.

Variable	Description
xAxis	A 2-dimensional matrix with the lateral coordinate for each pixel in units of millimeters.
zAxis	A 2-dimensional matrix with the depth coordinate for each pixel in units of millimeters.
timeAxis	A vector with timestamps for each ultrasound frame, in seconds.
hr	Subject's estimated heart rate during the scan in beats per second.
hrTimes	The estimated time for the beginning and ending of each cardiac cycle during scanning.
displacement	A 3-dimensional matrix of tissue displacement in units of millimeters.
displacementNorm	Displacement data broken up into individual cardiac cycles where each cardiac cycle has been stretched or shrunken to be an equivalent number of frames.

bMode	A 3-dimensional matrix of “Brightness” of the received ultrasound data used for determining tissue structure.
bModeNorm	Similar to displacementNorm with one bMode frame for each cardiac cycle.
bloodMask	Mask of blood in the brain derived from CT data registered to the ultrasound imaging plane.
bloodMaskThick	Probability mask of blood in the brain derived from CT data registered to the ultrasound imaging plane.
skullMask	Mask of the skull derived from CT data registered to the ultrasound imaging plane.
skullMaskThick	Probability mask of the skull derived from CT data registered to the ultrasound imaging plane.
ventMask	Mask of the ventricles derived from CT data registered to the ultrasound imaging plane.
ventMaskThick	Probability mask of the ventricles derived from CT data registered to the ultrasound imaging plane.
brainMask	Mask of the brain derived from CT data registered to the ultrasound imaging plane.
transPos	Position and orientation of the ultrasound transducer in CT space.
dataCT	The CT slice that is estimated to correspond to the ultrasound data. This is in Hounsfield units.

Patients’ CT images, used for initial diagnosis, were obtained, and aligned with the ultrasound planes to create the brain masks, skull masks, ventricle masks, and blood (intracranial hemorrhage) masks for each ultrasound plane. This process is called registration.

One thing to note is that the coordinates in this data have been transformed from polar coordinates to Cartesian coordinates. Initially the position of each pixel is characterized by its radial distance from the origin and its angle with respect to a line normal to the face of the transducer. After transformation the xAxis and zAxis are represented in Cartesian coordinates.

The most relevant variable for the purpose of this work is displacementNorm as it is used to develop representations of displacement in the brain over the cardiac cycle.

3.4 DATA PROCESSING

The aim of data processing is to determine a method of representing displacement data with the goal of comparing displacement between TBI and healthy subjects and identifying features that would help to detect the presence of intracranial hemorrhage.

3.4.1 *Averaging Displacement Data*

The first method utilized was to calculate an average displacement. Every pixel in a scan was averaged to one value with no additional processing. This was repeated for every scan over a cardiac cycle and the resulting waveform was plotted.

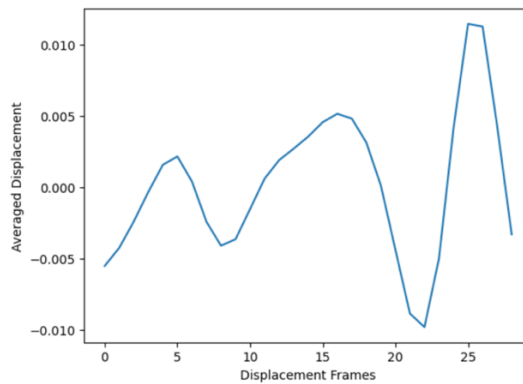


Figure 3.5 Averaged displacement waveform over a cardiac cycle for subject DoD126.

The issue with this strategy is that every part of the brain does not displace in the same direction. The two hemispheres in the brain displace contralaterally and so averaging the displacements causes a cancelling out effect. This means that this strategy would not be able to consistently determine how the whole brain's displacement is actually changing over time.

3.4.2 *Quadrant Displacement Data*

Another strategy utilized was to divide the displacement matrix into quadrants. This was an attempt to handle the contralateral displacement as well as the variation in time of blood flow; generally, the front of the brain fills before the back of the brain. However, this did not work because the brain is not centered in the scan or displacement matrix. So, the quadrants did not capture the quadrants of the brain as intended.

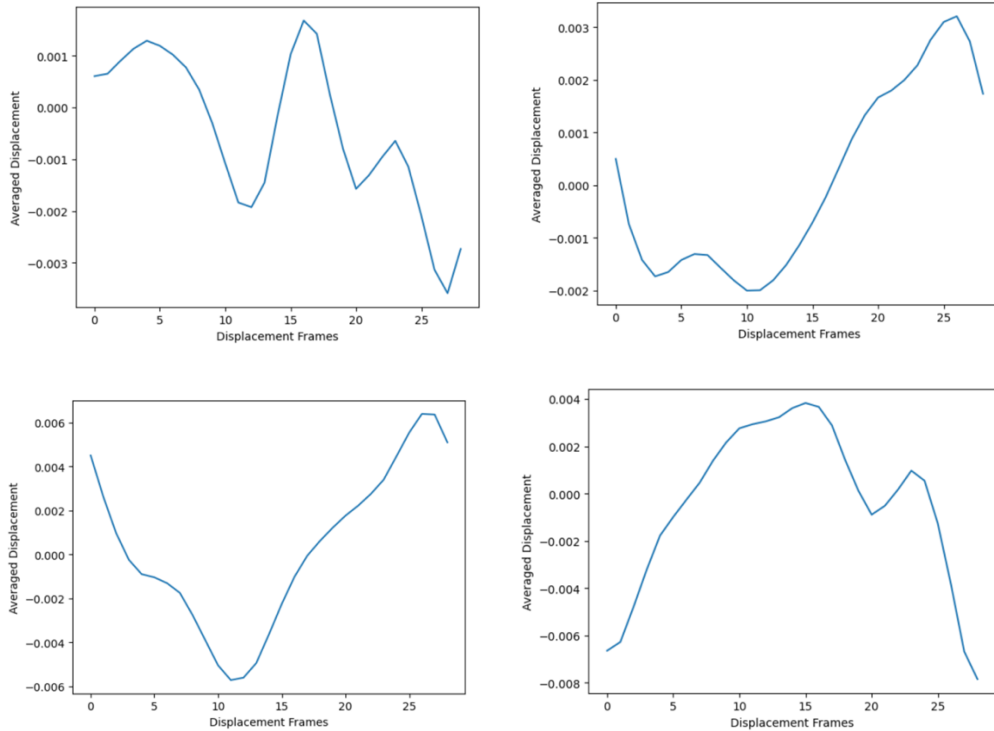


Figure 3.6 Averaged displacement waveform of the four quadrants for subject DoD001.

3.4.3 *Representative Displacement*

Finally, a representative displacement waveform was calculated using a method developed by Dr. John Kucewicz of the UW research team [22]. Representative displacement is meant to represent the average pulsatile waveform. The steps of the method are shown in figure 3.7. Representative displacement handles contralateral displacement of the brain by inverting pixels that are negatively correlated with the mean waveform of a given scan so that the direction of all the pixels are correlated and do not cancel out when averaged. As the direction of displacement is defined relative to the transducer, a significant detail of the data is that without further processing the representative displacement waveform can indicate that the beginning of the cardiac cycle, when the brain has emptied of blood and is beginning to fill, is the point of maximum displacement. To account for this when the start of the cardiac cycles is defined, the orientation of the waveform is defined such that the start of the cardiac cycle is a minimum point of displacement. The maximum point of displacement in the cardiac cycle is defined as occurring when the brain has completely filled with blood.

The peaks on one side of the waveform are going to be when it starts filling. The peaks on the other side are going to be when it starts draining. Differentiating between these peaks is necessary. In general, the blood fills faster than it drains. Looking at the timing between pairs of positive and negative peaks one can determine which are the filling peaks and which are the draining peaks, based on the timing between the pairs of peaks. Using this information about how blood flows into and out of the brain, an estimation of the beginning of the cardiac cycles is determined and the waveform is inverted based on these estimations. Figures 3.8 and 3.10 show the representative displacement waveform using normalized displacement data, developed in this project. Figures 3.19 and 3.11 show the waveforms developed by Dr. Kucewicz from non-normalized displacement data. The idea behind using representative displacement to better understand intracranial hemorrhage in TBI patients, is that intracranial hemorrhage influences vascular resistance and alters waveforms locally within the brain.

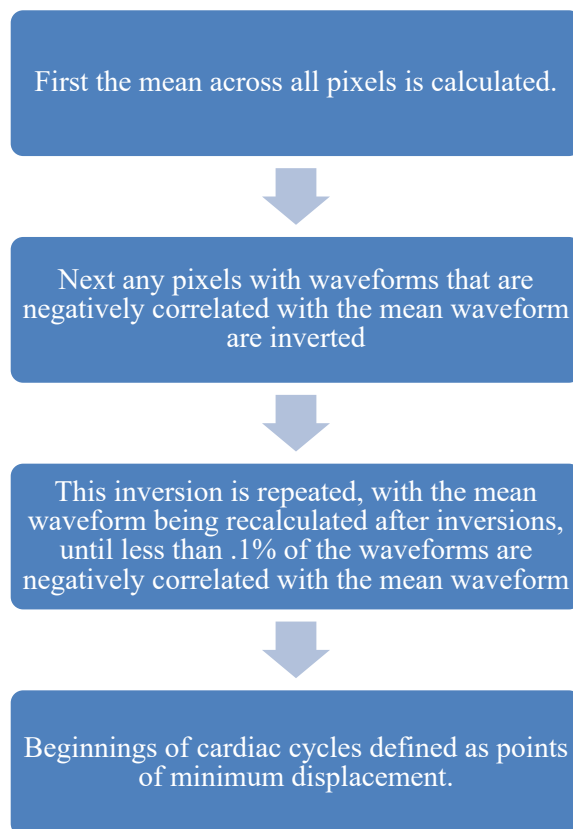


Figure 3.7 Greedy algorithm for calculating representative displacement [22].

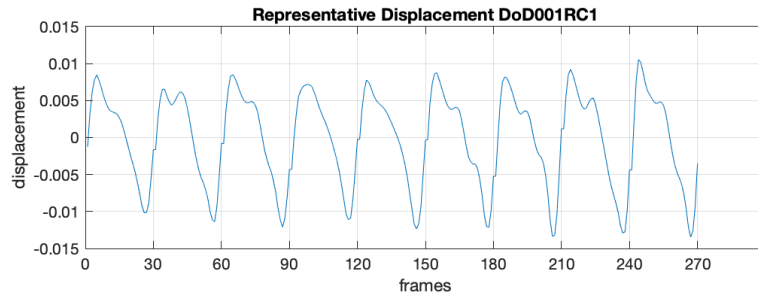


Figure 3.8 Representative displacement waveform for patient DoD001 for the first right cranial scan.

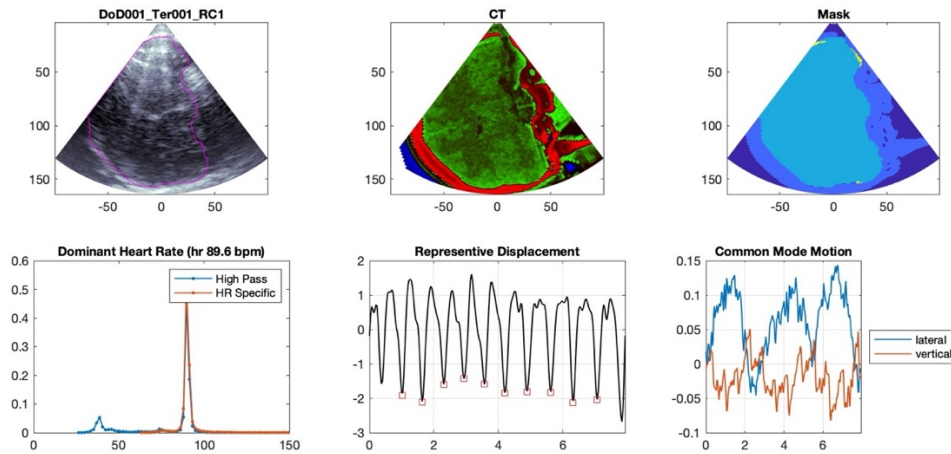


Figure 3.9 Patient DoD001 right coronal B-Mode scan (top left), CT scan (top middle), brain, skull, and blood masks (top right), heart rate (bottom left), representative displacement waveform (bottom middle), common mode motion (bottom right) [22].

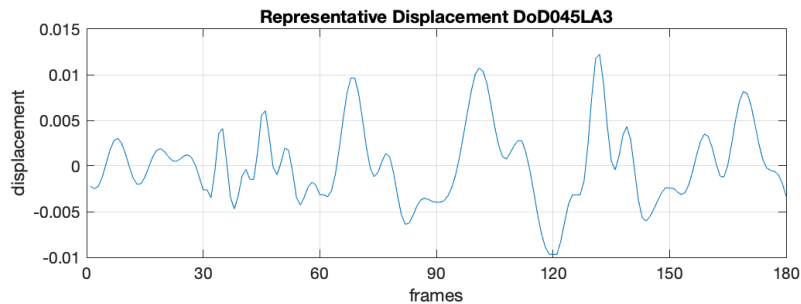


Figure 3.10 Representative displacement waveform for patient DoD0045 for the third left axial scan.

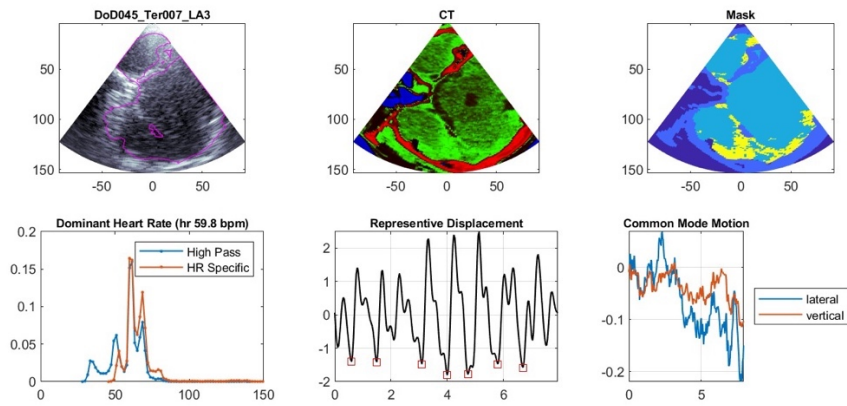


Figure 3.11 Patient DoD045 left axial B-Mode scan (top left), CT scan (top middle), brain, skull, and blood masks (top right), heart rate (bottom left), representative displacement waveform (bottom middle), common mode motion (bottom right) [22].

Chapter 4. RESULTS

Analysis of representative displacement data was conducted in this research. Sources of noise in the data as well as initial data pipeline setup will be discussed. Results from maximum displacement frame analysis and principal component analysis will also be discussed in this section. Results of analysis for each scan angle (right axial (RA), right coronal (RC), left axial (LA), left coronal (LC)) were kept separated to identify any differences that may exist between the scan angles. TBI data will be compared to healthy data, and a subset of TBI data which only includes Intraparenchymal Hemorrhage data will be compared to healthy data. This injury type was identified as being the most severe and potentially this data is the most different from the healthy data. The subset Intraparenchymal data will also be compared to the rest of the TBI data, this comparison is done to observe any differences within the TBI data.

4.1 NOISE IN DATA

Some of the representative waveforms were particularly noisy. The source of this noise that was not removed by the common mode motion correction, which is intended to remove noise due to general movement. This noise may potentially be caused by imaging through the skull. The skull attenuates ultrasound signals and creates noise in the data, and so can pose challenges in this research. The properties of the skull can also vary between individuals so the level of signal attenuation can vary between individuals. Which is why some subjects had noisier data while others did not. Additionally common mode motion correction may not have been able to address common mode motion. Very large movements by the patient relative to the scanner could introduce more noise than can be processed. Figure 4.1 shows large lateral and vertical spikes in the common mode motion that may not have been able to be handled by signal processing, resulting in noise in the representative displacement waveform.

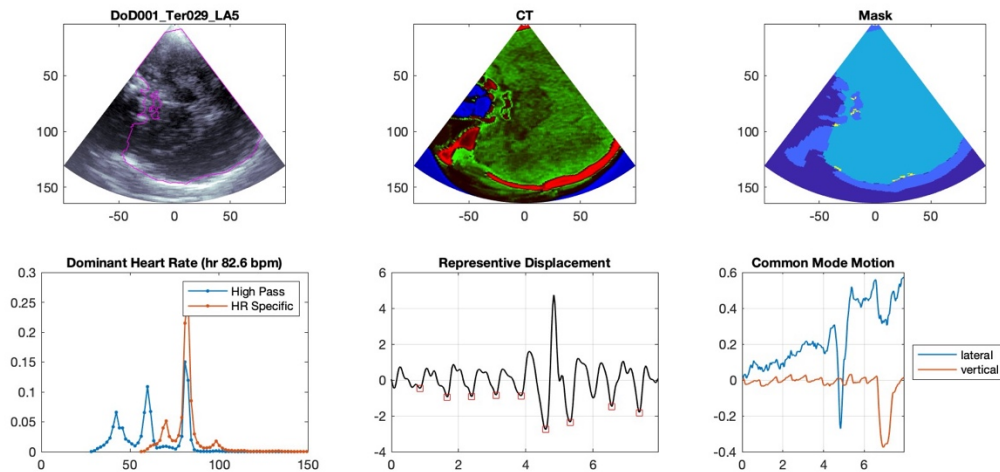


Figure 4.1 Patient DoD001 left axial B-Mode scan (top left), CT scan (top middle), brain, skull, and blood masks (top right), heart rate (bottom left), representative displacement waveform (bottom middle), common mode motion (bottom right).

4.2 DATA PROCESSING PIPELINE

An initial data processing pipeline was developed to learn how to work with the data and better understand the structure of the data. The representative displacement waveforms for the TBI patients were condensed into one averaged cardiac cycle. The averaged cardiac cycles for a particular patient and for a particular scan angle were then averaged together. This meant that each patient had one averaged cardiac cycle of displacement for each scan angle. This same process was also completed for the healthy subjects. Additionally, the healthy subject cardiac cycle waveforms were averaged for the 12 subjects. This resulted in one waveform for every scan angle that was representative of all 12 subjects. The pipeline for TBI data can be seen in figure 4.2. The pipeline for healthy data can be seen in figure 4.3.

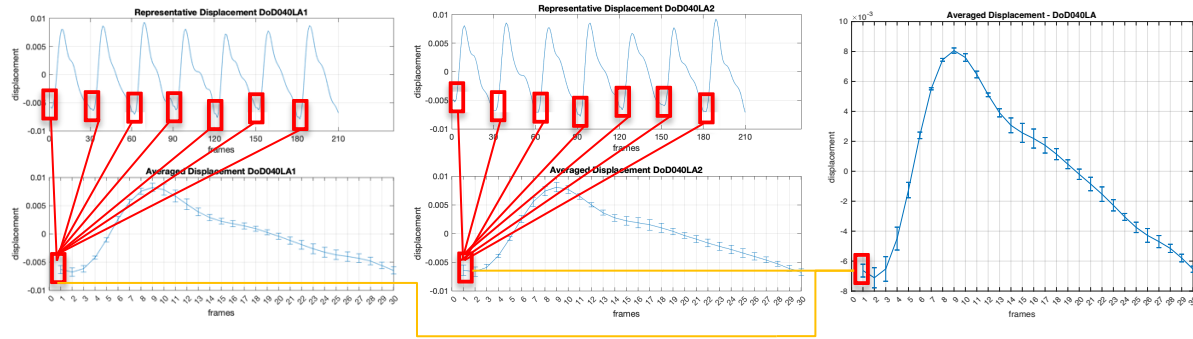


Figure 4.2 On the left is the representative displacement waveform for TBI patient DoD040 for the first left axial scan. In the middle is the waveform for patient DoD040 for the second left axial scan. The full waveforms are on the top and the condensed single cardiac cycle waveforms are on the bottom. On the right is the averaged single cardiac cycle for all left axial scans for DoD040. Error bars show the standard deviation of averaged displacement frames.

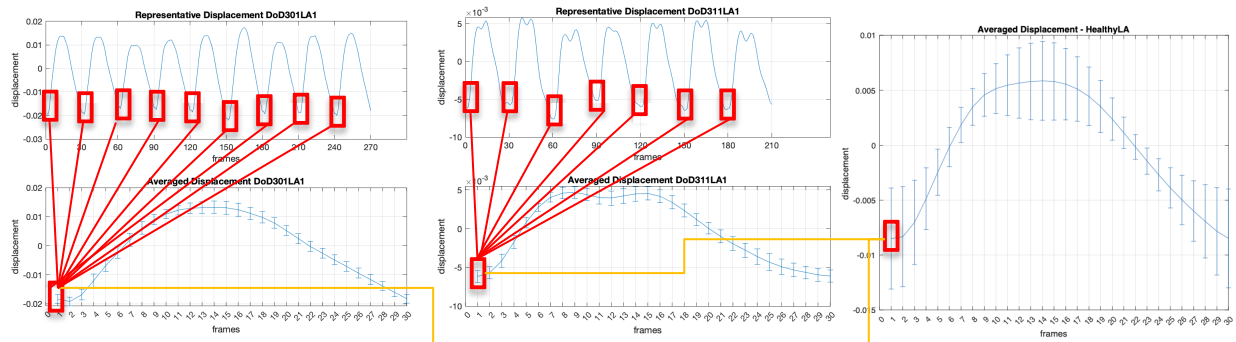


Figure 4.3 On the left is the representative displacement waveform for TBI patient DoD301 for the left axial scan. In the middle is the waveform for patient DoD311 for the left axial scan. The full waveforms are on the top and the condensed single cardiac cycle waveforms are on the bottom. On the right is the averaged single cardiac cycle for all healthy patients for the left axial scan angle. Error bars show the standard deviation of averaged displacement frames.

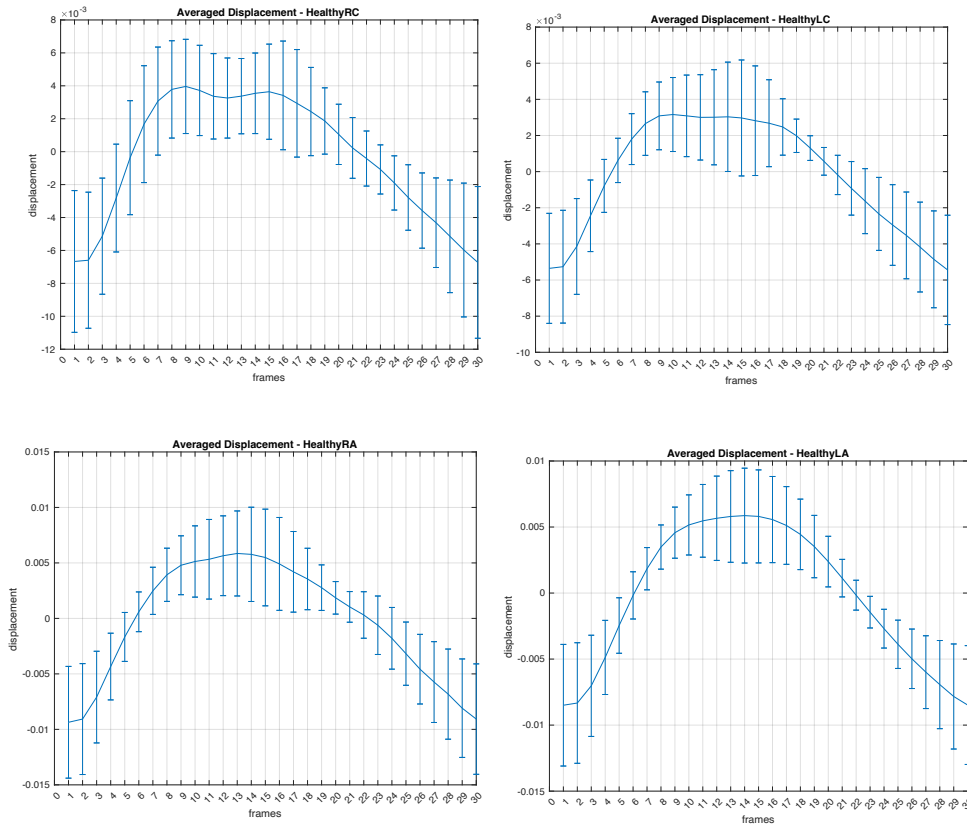


Figure 4.4 Condensed and averaged representative displacement data for all healthy patients at the four different scan angles. Error bars show the standard deviation of the averaged individual healthy data.

After looking at the condensed and averaged data, the standard deviation is very large compared to averaged displacement. Condensing and averaging the data may cause a loss in information such as the variance of the data. For PCA this approach was not utilized, and a different method was chosen to process the data.

4.3 MAXIMUM DISPLACEMENT ANALYSIS

One of the original goals of this project was to identify the maximum frame of brain displacement due to blood flow, to utilize as input into image segmentation models for identifying intracranial hemorrhage. Using representative displacement data, the maximum frame of displacement for every patient at every scan angle was identified. The occurrence of every displacement frame as the frame containing maximum displacement is counted and displayed in

figures 4.9 and 4.10. Figure 4.11 shows the average maximum displacement frame for healthy and TBI data for every scan angle.

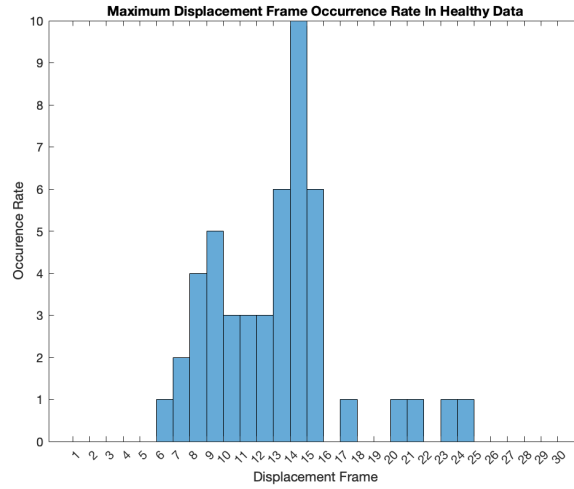


Figure 4.5 Occurrence rate of maximum displacement frame in healthy data.

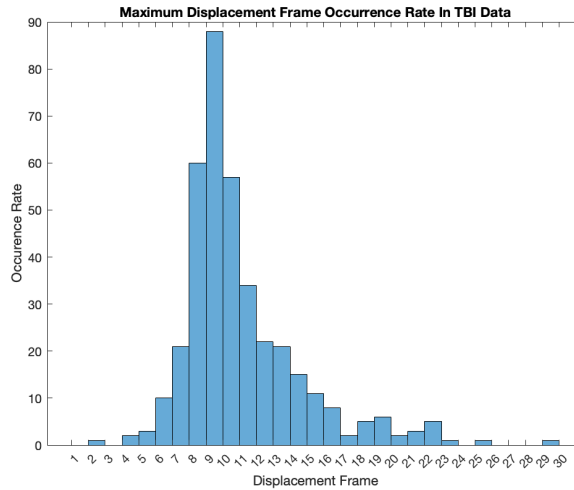


Figure 4.6 Occurrence rate of maximum displacement frame in healthy data.

Table 4.2. The average maximum displacement frame and standard deviation for healthy and TBI data for every scan angle.

	Average of Max Healthy	Standard Deviation of Max Healthy	Average of Max TBI	Standard Deviation of Max TBI
Right Coronal	10.50	3.26	10.51	3.54
Right Axial	13.17	3.88	11.31	3.99
Left Coronal	14.25	4.41	10.40	3.25
Left Axial	12.83	3.51	10.06	3.31

T-Tests are a ratio that quantifies how significant the difference is between the 'means' of two groups while taking their variance or distribution into account [23]. The distribution for the T-Tests was specified as two-tailed, and the kind of T-Test performed was two-sample unequal variance.

Results can be seen in table 4.3. The alpha level used for this analysis is .05. The left coronal and left axial T-Tests have a p-value of less than .05. It can be concluded that the difference between the frames of maximum displacement of the two groups for those scan angles is statistically significant.

Table 4.3. Results of T-Tests comparing frames of maximum displacement for TBI and healthy data.

T-Test RC	T-Test RA	T-Test LC	T-Test LA
0.996	0.145	0.012	.022

For the healthy data the point of maximum displacement is more likely to be later in the cardiac cycle. Looking at the occurrence rate, frame 14 is most often the maximum displacement frame and frames 13 and 15 are second in occurrence rate. For the TBI data the point of maximum displacement is more likely to be earlier in the cardiac cycle. Looking at the occurrence rate frame 9 is most often the maximum displacement frame, frame 10 is second, and 8 is third in occurrence rate. Observing the averages, the same pattern is apparent. The differences for left coronal and left axial are statistically significant.

4.4 PRINCIPAL COMPONENT ANALYSIS

Principal component analysis (PCA) is a linear projection method based on singular value decomposition (SVD) [24]. PCA is an unsupervised learning method that facilitates data clustering and dimensionality reduction. The transformation process provides information that facilitates the identification of relevant properties of the data and possible correlations between them.

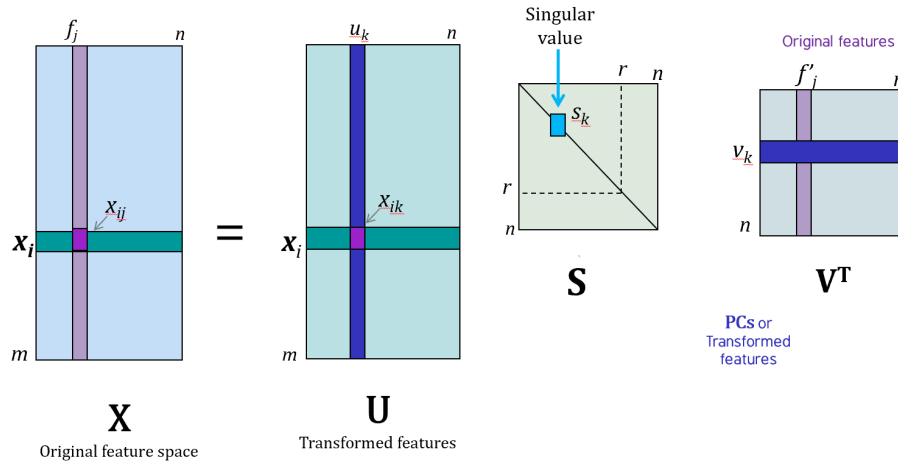


Figure 4.7 Components of Singular Value Decomposition (SVD) [24].

The input for SVD is the observation matrix X [24]. In this matrix, rows are observations and columns are features. The first output or factor is U which contains the observations in a new transformed space. Rows are observations and columns are principal components (PC). The next output is S . S contains the singular values along the diagonal which are the weights of each PC. The last output is V transposed which maps between the original features and the transformed features.

The outputs of PCA observed in this analysis are scree plots, cumulative scree plots, loading vectors, and scatter plots. The scree plots are a line plot of the singular values of PCs, singular values are the “weight” of each new PC and is an indication of how much information is retained by each PC [24]. The cumulative scree plots show the cumulative contribution of the PCs to the explanation of variance in the data. The loading vectors show how much each original feature contributes to a PC and which features are correlated. The loading vectors are shown as bar graphs, where the magnitudes of each component come from each column vector of V . From the magnitude it is possible to determine the importance of that feature in the makeup of that PC. Also, by comparing the magnitudes of each feature with the others, the correlation between features can be assessed. The scatter plots show the new transformed features i.e., PCs. The scatter plots are created by plotting the first k relevant PCs of the matrix U to see observations in new space. The scatter plots help to observe clusters.

For input into PCA the data was broken up into individual cardiac cycles, from a series of cardiac cycles. This was done for every subject, both healthy and TBI, and then every cardiac cycle was used as a separate observation for PCA. The features are the 30 displacement frames over the cardiac cycle. As is standard procedure the original data was also preprocessed so that each feature column is mean centered (has a mean of 0) and its variance is normalized (unit variance).

The scree plots, cumulative scree plots, and loading vectors for TBI data at every scan angle and healthy data at every scan angle will be analyzed. Then the scatter plots of TBI and healthy data, scatter plots of only IPH and healthy data, and scatter plots of IPH and non-IPH TBI data will be discussed.

4.4.1 Only TBI Loading Vectors and Scree Plots

Figure 4.8 shows the scree plot and cumulative scree plot from PCA with right coronal TBI data. PC1 accounts for about 41% of the variance in the data, PC2 about 26%, PC3 about 14%, and PC4 about 9%. With 4 principal components about 90% of the variance in the data can be explained.

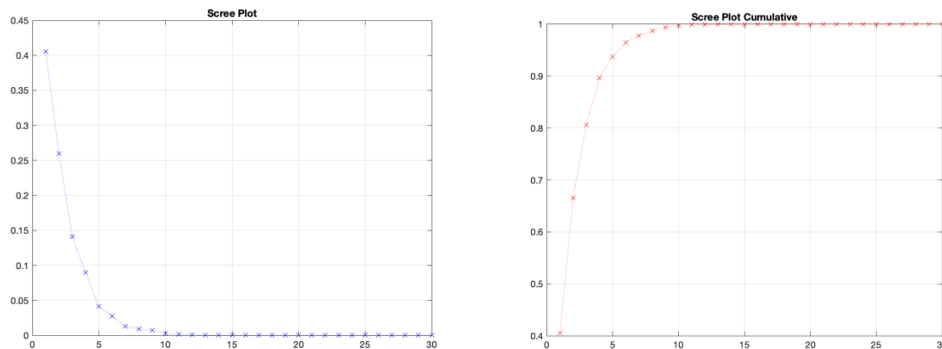


Figure 4.8 Right coronal only TBI, Scree Plot and Cumulative Scree Plot

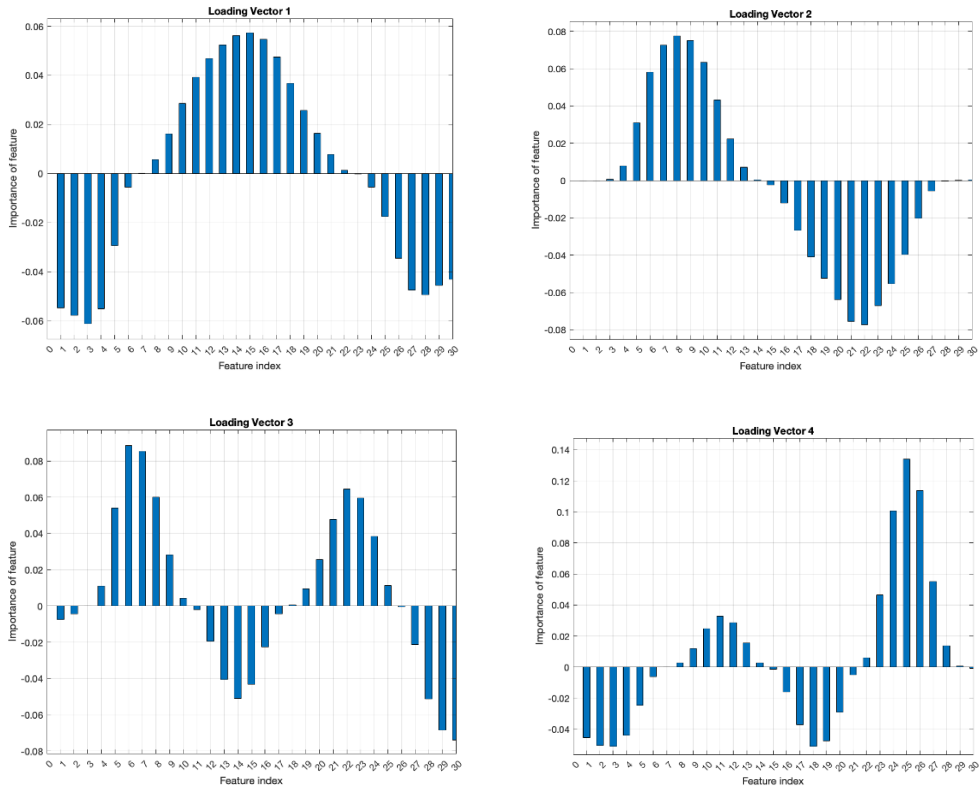


Figure 4.9 Right coronal only TBI, first four loading vectors

Figure 4.10 shows the scree plot and cumulative scree plot from PCA with right axial TBI data. PC1 accounts for about 43% of the variance in the data, PC2 about 26%, PC3 about 12%, and PC4 about 9%. With 4 principal components about 90% of the variance in the data can be explained.

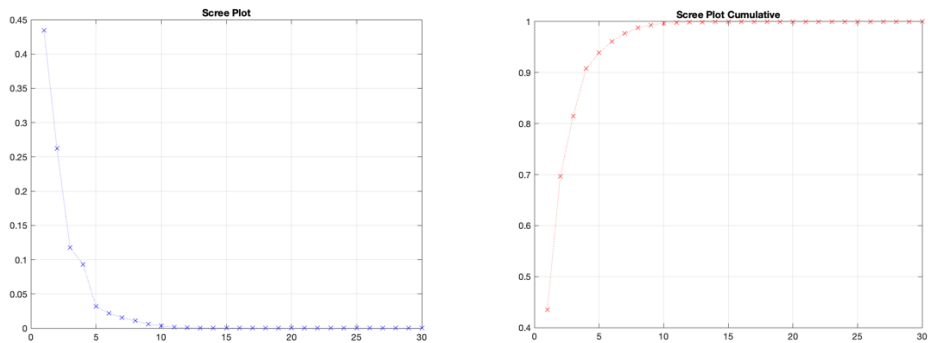


Figure 4.10 Right axial only TBI, Scree Plot and Cumulative Scree Plot

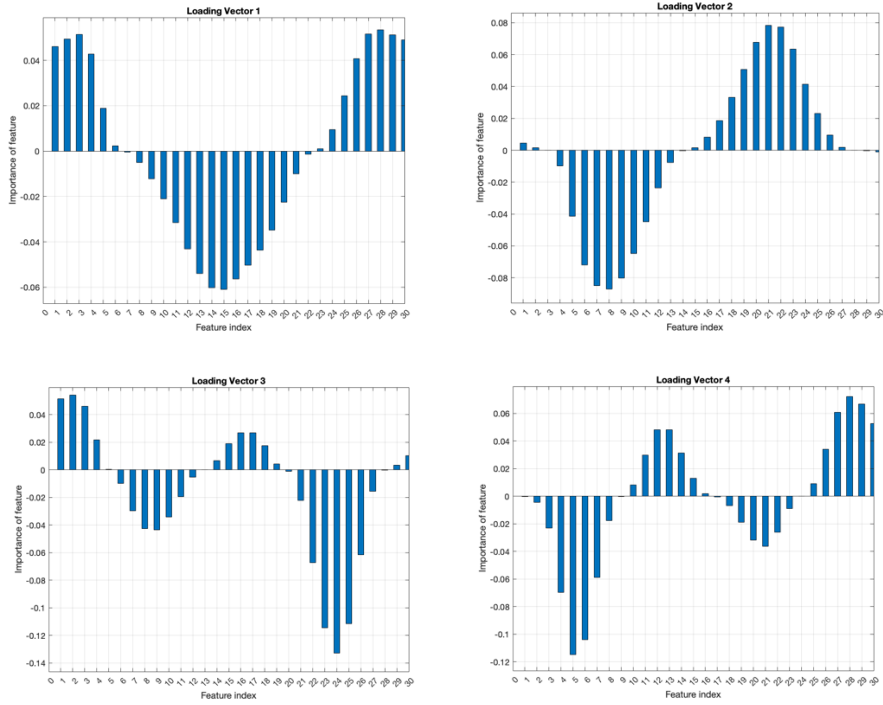


Figure 4.11 Right axial only TBI, first four loading vectors

Figure 4.12 shows the scree plot and cumulative scree plot from PCA with left coronal TBI data. PC1 accounts for about 41% of the variance in the data, PC2 about 30%, PC3 about 10%, and PC4 about 8%. With 4 principal components about 89% of the variance in the data can be explained.

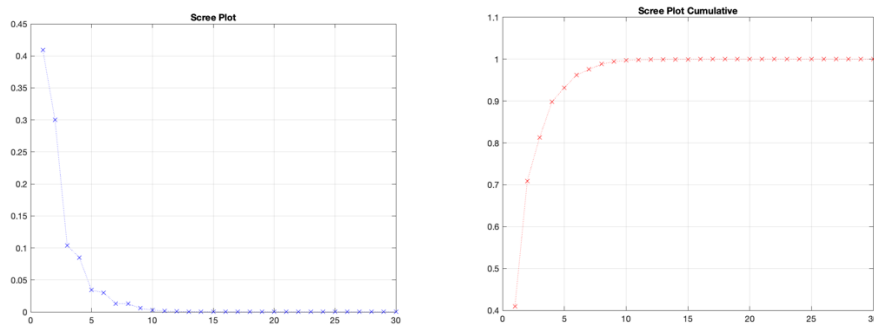


Figure 4.12 Left coronal only TBI, Scree Plot and Cumulative Scree Plot

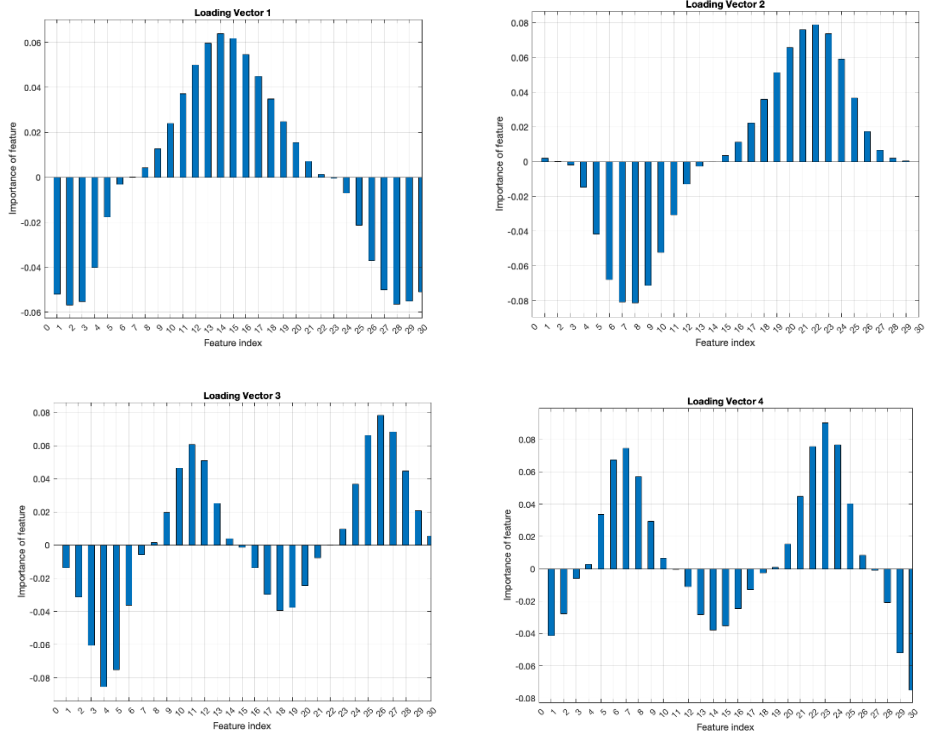


Figure 4.13 Left coronal only TBI, first four loading vectors

Figure 4.14 shows the scree plot and cumulative scree plot from PCA with left axial TBI data. PC1 accounts for about 41% of the variance in the data, PC2 about 31%, PC3 about 10%, and PC4 about 8%. With 4 principal components about 90% of the variance in the data can be explained.

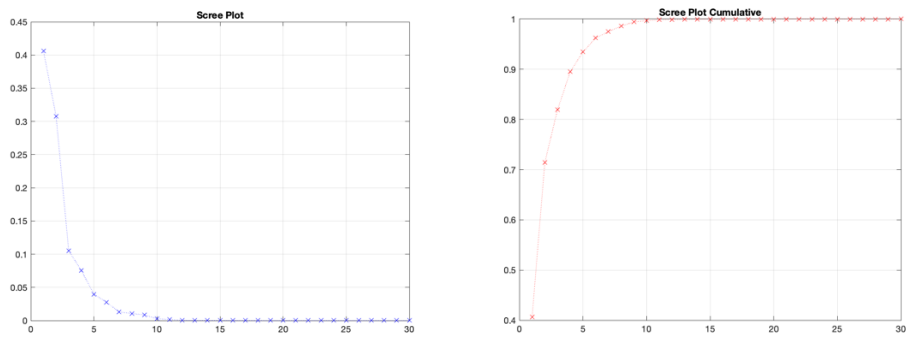


Figure 4.14 Left axial only TBI, Scree Plot and Cumulative Scree Plot

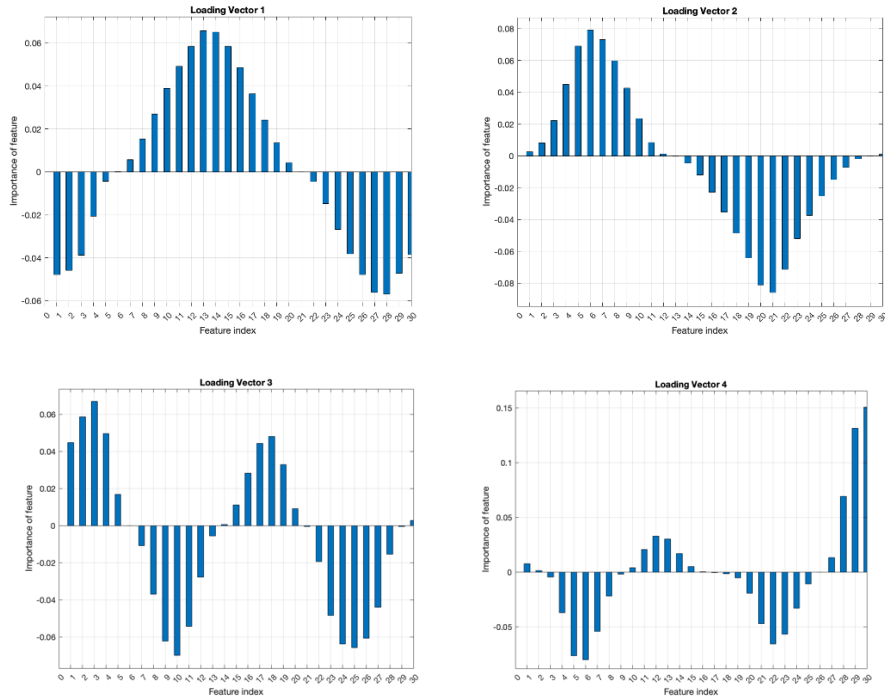


Figure 4.15 Left axial only TBI, first four loading vectors

4.4.2 Only Healthy Loading Vectors and Scree Plots

Figure 4.16 shows the scree plot and cumulative scree plot from PCA with right coronal healthy data. PC1 accounts for about 50% of the variance in the data, PC2 about 27%, PC3 about 7%, and PC4 about 5%. With 4 principal components about 89% of the variance in the data can be explained.

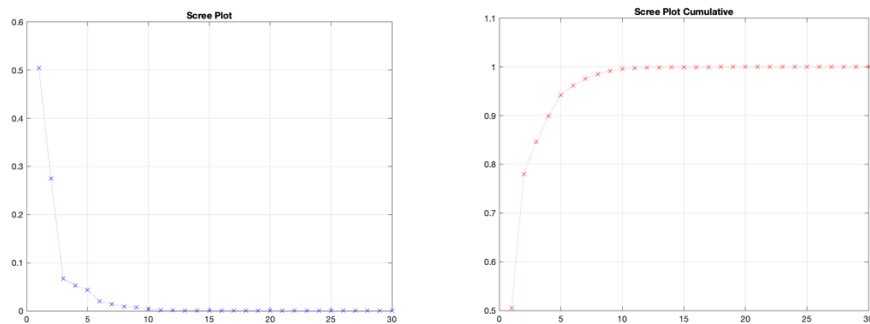


Figure 4.16 Right coronal only healthy, Scree Plot and Cumulative Scree Plot

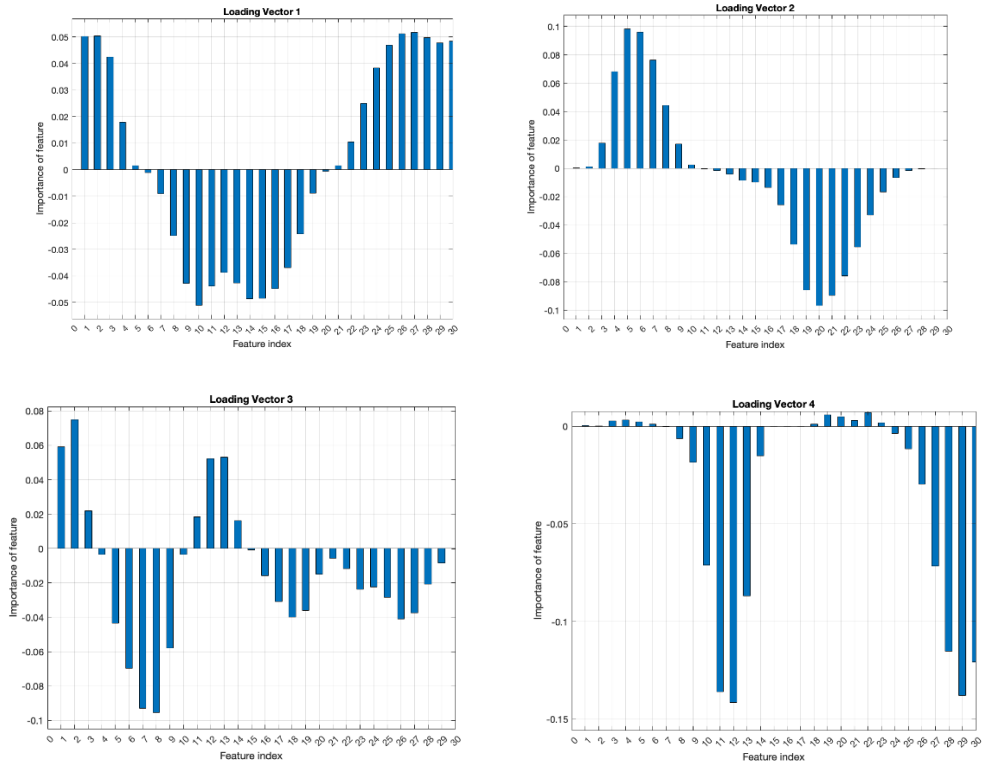


Figure 4.17 Right coronal only healthy, first four loading vectors

Figure 4.18 shows the scree plot and cumulative scree plot from PCA with right axial healthy data. PC1 accounts for about 54% of the variance in the data, PC2 about 20%, PC3 about 12%, and PC4 about 4%. With 4 principal components about 90% of the variance in the data can be explained.

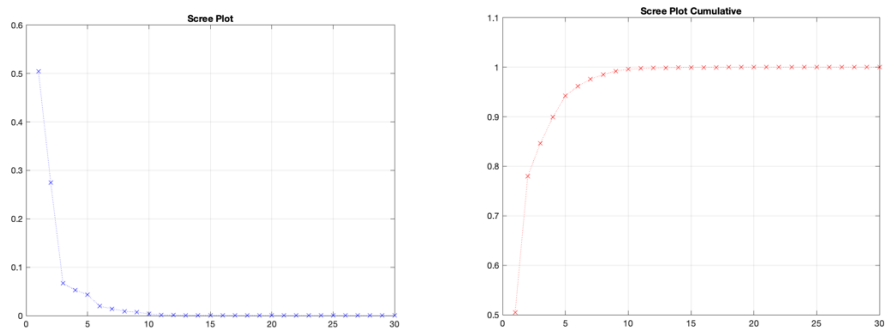


Figure 4.18 Right axial only healthy, Scree Plot and Cumulative Scree Plot

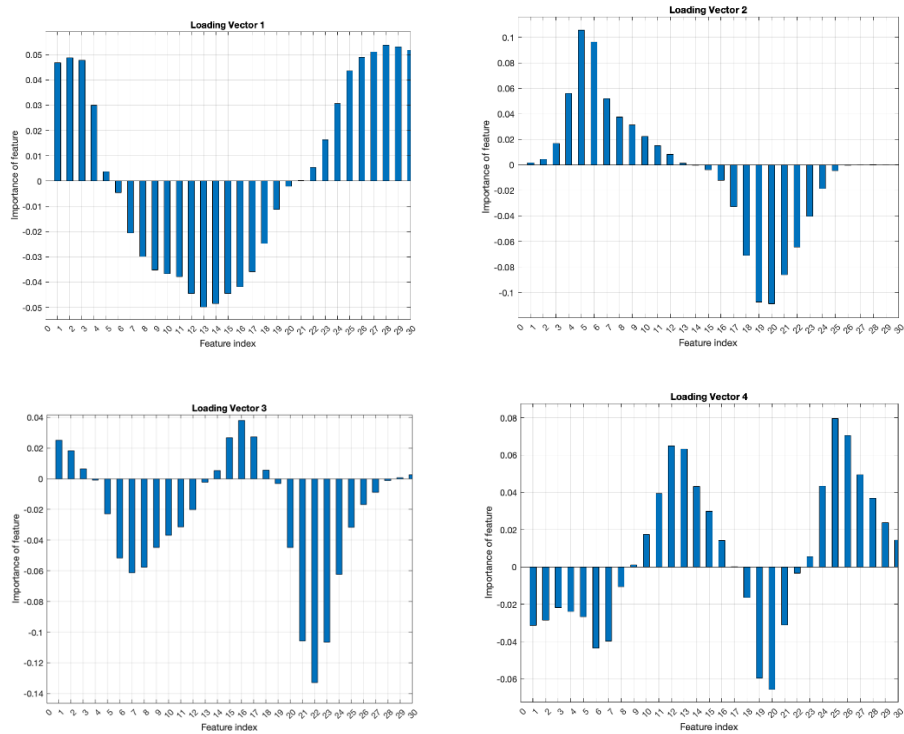


Figure 4.19 Right axial only healthy, first four loading vectors

Figure 4.20 shows the scree plot and cumulative scree plot from PCA with left coronal healthy data. PC1 accounts for about 56% of the variance in the data, PC2 about 21%, PC3 about 8%, and PC4 about 4%. With 4 principal components about 89% of the variance in the data can be explained.

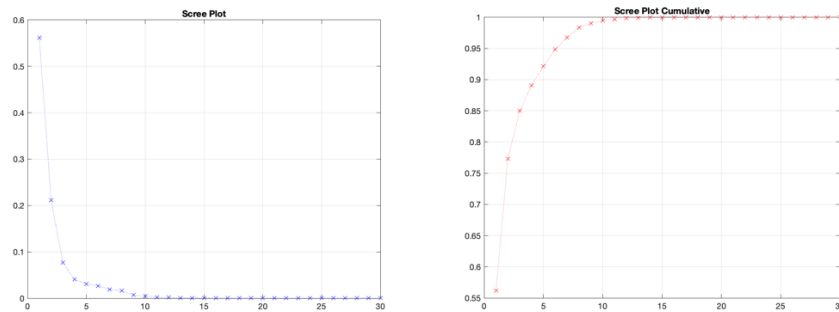


Figure 4.20 Left coronal only healthy, Scree Plot and Cumulative Scree Plot

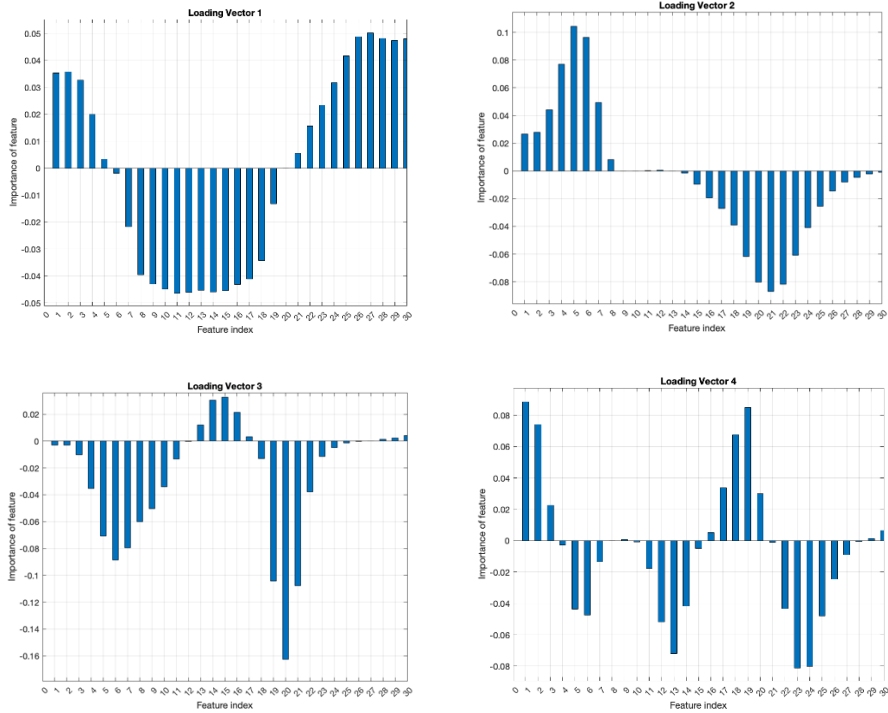


Figure 4.21 Left coronal only healthy, first four loading vectors

Figure 4.22 shows the scree plot and cumulative scree plot from PCA with left axial healthy data. PC1 accounts for about 53% of the variance in the data, PC2 about 32%, PC3 about 7%, and PC4 about 4%. With 4 principal components about 96% of the variance in the data can be explained.

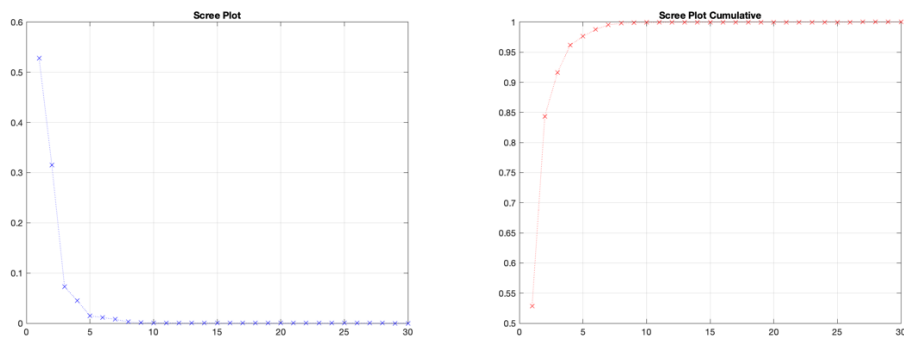


Figure 4.22 Left axial only healthy, Scree Plot and Cumulative Scree Plot

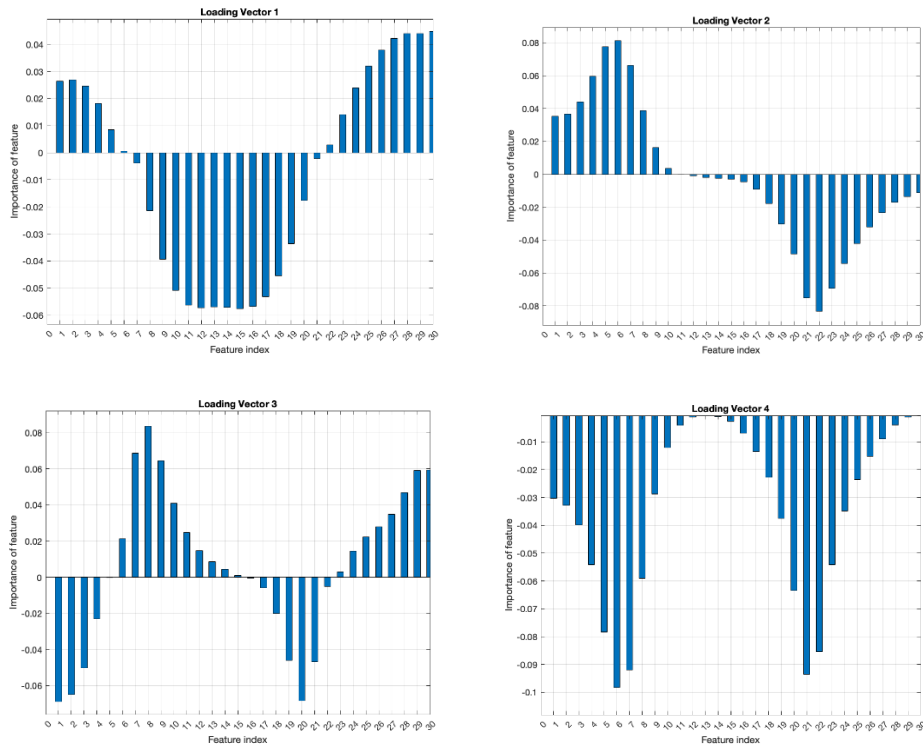


Figure 4.23 Left axial only healthy, first four loading vectors

For both healthy and TBI data the first four principal components explain about 89-90% of the variability in the data. However, for the healthy data the first principal component explains consistently more of the variance in the data, about 50-56%, as compared to the TBI data, about 41-43%. This is likely due to the healthy data having less variability but also the healthy data being a much smaller sample size.

Looking at the loading vectors for the TBI data, across the scan angles the pattern of feature distribution in the loading vectors is similar. The healthy data has a similar form of distribution as the TBI data, but the patterns of magnitudes are different. Further analysis of this trend is needed.

4.4.3 Weakest Loading Vectors

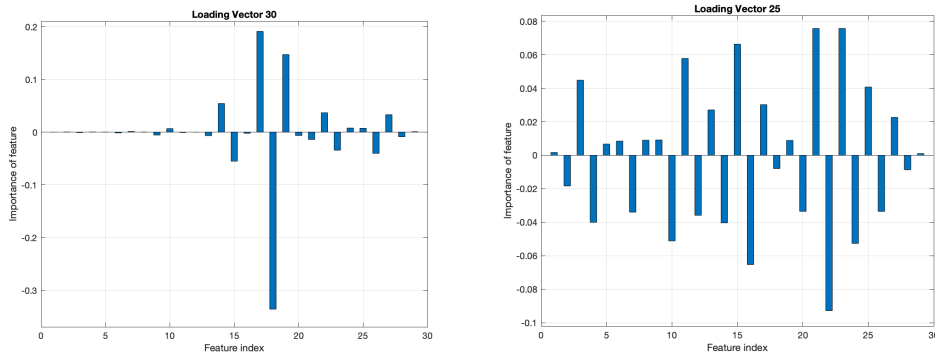


Figure 4.24 Weakest loading vectors for TBI data.

Compared to the loading vectors for stronger principal components the weaker loading vectors do not follow the same wave-like distribution. The distribution of feature magnitude appears much noisier.

4.4.4 Healthy vs TBI PCA Scatter Plots With Strongest Clustering

Figures 4.25-4.29 show scatter plots from PCA with healthy and TBI data. Healthy data points are shown as red circles and TBI data points are shown as blue dots. These scatter plots show that there is promising clustering within the healthy data points. This is likely due to the healthy data being more similar than the TBI data.

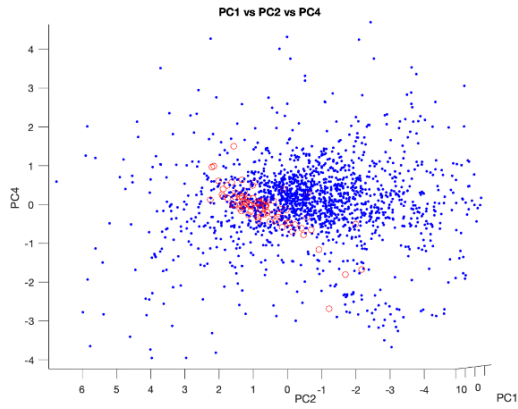


Figure 4.25 Healthy and TBI Right Coronal

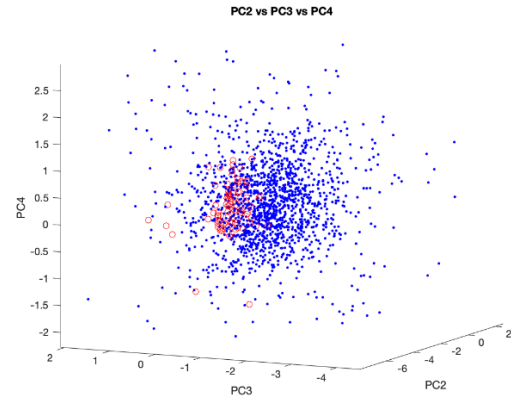


Figure 4.26 Healthy and TBI Left Axial

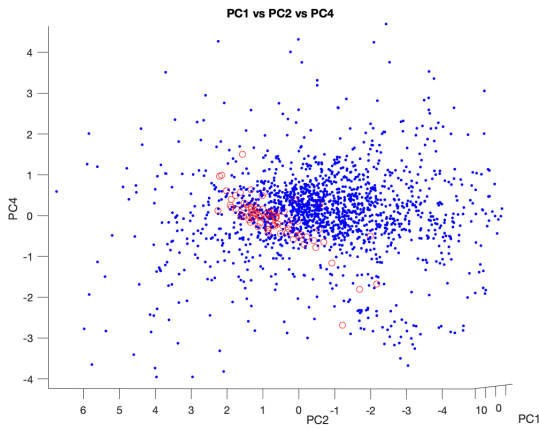


Figure 4.27 Healthy and TBI Right Coronal

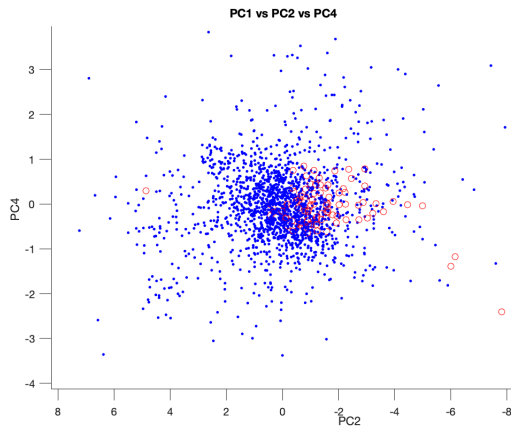


Figure 4.28 Healthy and TBI Left Axial

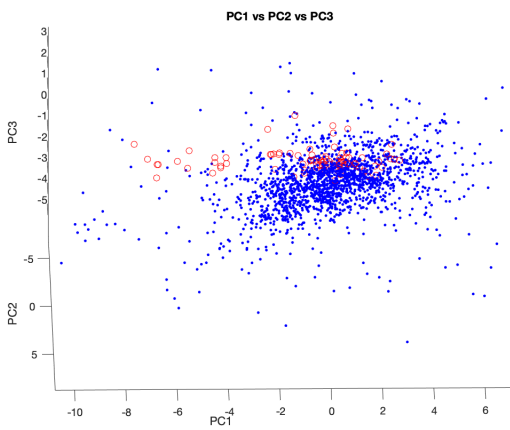


Figure 4.29 Healthy and TBI Left Axial

4.4.5 Healthy vs TBI PCA Scatter Plots With Weakest Principal Components

Figures 4.30 and 4.31 show scatter plots from PCA with healthy and IPH data. These show the weakest principal components, which explain the least amount of variance in the data. Preliminary results show some clustering with the TBI data, this is surprising as these are the weakest principal components in the scatter plot. Further analysis is needed to understand this behavior.

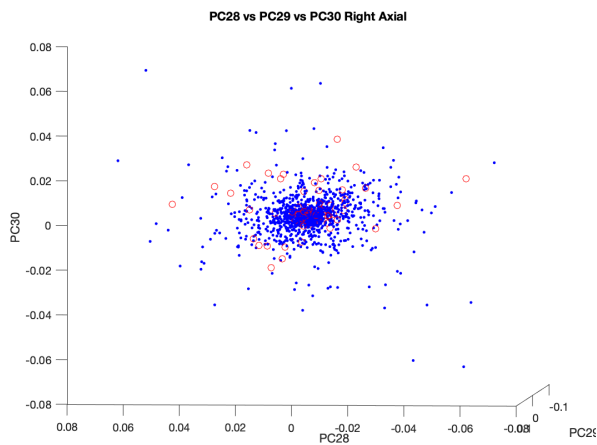


Figure 4.30 Healthy and TBI RA

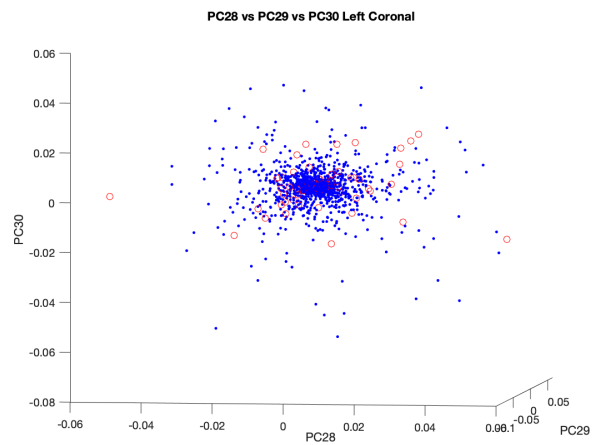


Figure 4.31 Healthy and TBI LC

4.4.6 Healthy vs IPH PCA Scatter Plots With Strongest Clustering

Figures 4.32 and 4.33 show scatter plots from PCA with healthy and IPH data. Healthy data points are shown as red circles and IPH data points are shown as blue dots. These scatter plots show again that there is promising clustering within the healthy data points. This is likely due to the healthy data being more similar than the IPH data. The clustering is more apparent in these plots as the healthy and IPH data are more balanced.

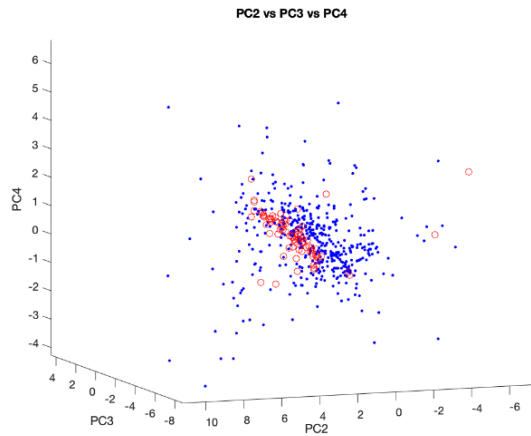


Figure 4.32 Healthy and IPH Right Axial

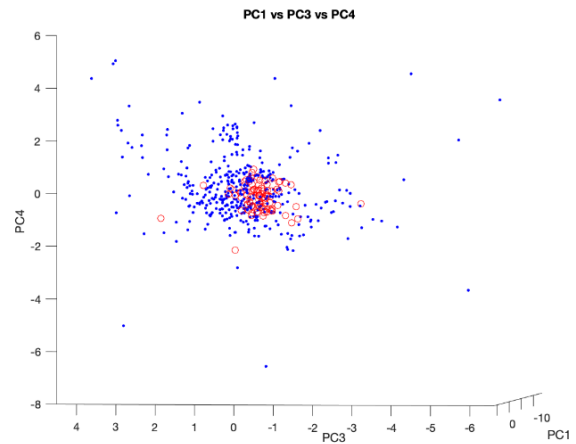


Figure 4.33 Healthy and IPH Left Axial

4.4.7 *IPH vs non-IPH PCA Scatter Plots*

Figures 4.34-4.37 show scatter plots from PCA with IPH and non-IPH TBI data. IPH data points are shown as red circles and non-IPH data points are shown as blue dots. These scatter plots do not show any preliminary promising clustering of IPH or non-IPH data. Further research is needed to determine if clustering of TBI subtypes is possible.

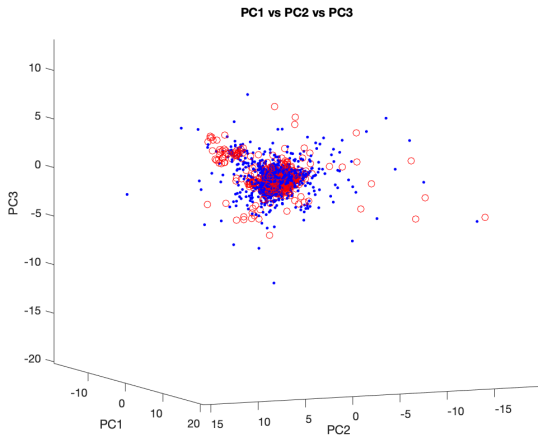


Figure 4.34 IPH and non-IPH Left Axial

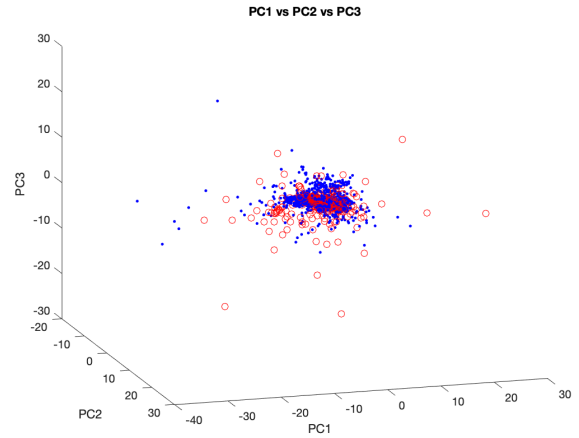


Figure 4.35 IPH and non-IPH Right Axial

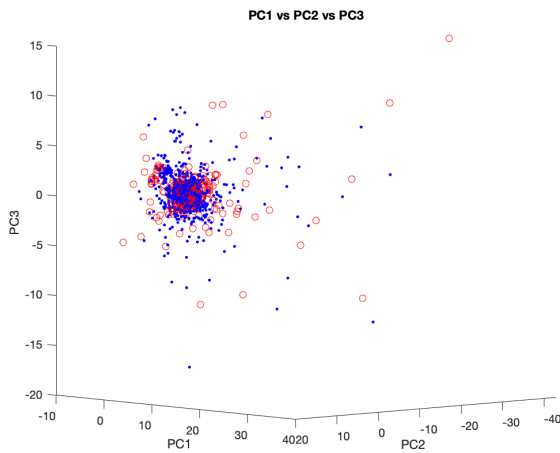


Figure 4.36 IPH and non-IPH Left Coronal

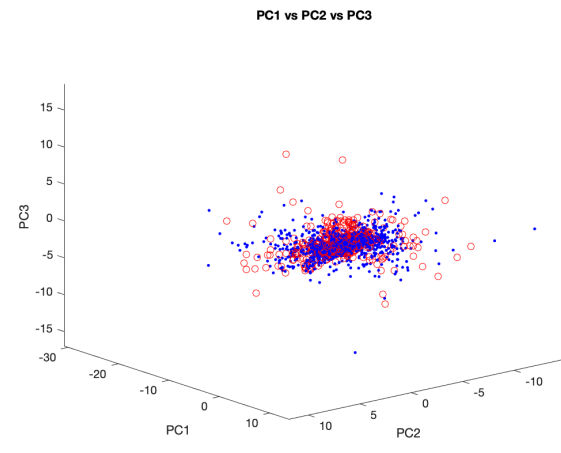


Figure 4.37 IPH and non-IPH Right Coronal

4.5 EXPERIMENTING WITH SUPPORT VECTOR MACHINE

In this section results of experiments are explored using support vector machines (SVM) as a classifier to try to distinguish between two classes. SVMs were chosen because results, presented in previous section 4.4 for PCA scatter plots, suggested that a linear classifier could be used on this data. SVM is a supervised learning algorithm that works particularly well with data that has linear behavior and is particularly useful in cases where the datasets are smaller. SVM builds an optimal hyperplane to separate the data into two categories [24]. This separating hyperplane is constructed in such a way that it maximizes the distance between the plane and the nearest data points from both classes. When there are points of one class crossed over the hyper-plane and

intersecting with the other class, this is considered an error. SVM seeks to minimize the distance of these error points from the correct side of the hyper-plane.

In this experiment only the healthy and IPH TBI data is used because this had the most balanced classes and the scatter plots in the previous section depict a clearer visual separation between the two classes and two clusters.

Based on the scree plots in the previous section, the first 5 PCs account for more than 90% of the total data variance. In here we present the results for SVM models using the first 5 PCs as input. Classification error was used as the metric to measure performance of the models. Classification error measures the inaccuracy of the model [25]. In Table 4.4 the SVM model used on right axial data misclassifies approximately 15.5% of the test data, on left axial data approximately 18.8%, on right coronal data approximately 17.5%, and on left coronal data the SVM model misclassifies approximately 17.9% of the test data. No parameter tuning or model optimization techniques were applied, so there is likely room for improvement. These results show promise for further application of SVM models on this data.

Table 4.4. Results of SVM for healthy and IPH TBI data.

	Right Axial	Left Axial	Right Coronal	Left Coronal
Classification Error	0.155	0.188	0.175	0.179

Chapter 5. CONCLUSION AND FUTURE WORK

The results of this work show that there are potentially features in representative displacement that can differentiate healthy and TBI data. Maximum displacement frame analysis shows that there is a statistically significant difference in time of maximum displacement between healthy and TBI data. PCA scatter plots show clustering of healthy data compared to TBI data. This could be due to healthy data having less variance. The scree plots showed that the first principal component explained more variance in healthy data compared to TBI data, again likely due to healthy data having less variance. Preliminary results do not show differentiation between IPH and non-IPH, more research is needed into TBI subtype clustering. Results from PCA also show original features that are highly correlated and that contribute most to the stronger principal components. Further exploration of dimensionality reduction could provide additional insight into the data. These results indicate that more data exploration is needed and that there is strong justification for the collection of more TBI and healthy data.

There were certain challenges throughout this work. This project lacked written documentation and lacked a central repository for information. A lot of details have been verbally shared but formalizing that documentation was something that this work aimed to do. Additionally, there was a lack of standards and consistent naming conventions in the documentation that did exist. This made it difficult to identify relevant sources for this research. Many researchers who previously worked on the TBI project have since left, this made communication more difficult. Much of the discussion with Dr. Kucewicz regarding this project occurred via email, which often led to misunderstanding and miscommunication. Much of this communication has now been formalized and documented so that it can be avoided in the future. The data used in this research is highly specialized and not having domain expertise in neuroscience was a challenge. Finally, the biggest challenge in this work was lack of data.

The results of this work are promising and open up many avenues for future work. First, additional data is needed, especially healthy data which is currently imbalanced compared to the TBI data. Without more data the results gathered cannot be applied to the general population. With the current data, more techniques to balance the datasets should be explored. For example, randomly sampling the TBI data, rather than inputting all of the data, or using the condensed data could prove useful when comparing to healthy data for PCA. TBI data collected closer to the time

of injury and diagnosis is also needed. Results of PCA show the need for further analysis of dimensionality reduction. This is promising research for the application of machine learning models. Further analysis using support vector machine is needed, especially with more visualizations, and k-Nearest Neighbor would be a good candidate for use with this data. Finally, independent component analysis (ICA) could be explored with this data. ICA assumes non-gaussian distribution and is used for waveform analysis and frequency decomposition.

BIBLIOGRAPHY

- [1] Centers for Disease Control and Prevention. (2022, December 15). *Traumatic Brain Injury & Concussion*. Centers for Disease Control and Prevention. Retrieved March 1, 2023, from <https://www.cdc.gov/traumaticbraininjury/index.html>
- [2] Mayo Foundation for Medical Education and Research. (2021, February 4). *Traumatic brain injury*. Mayo Clinic. Retrieved March 1, 2023, from <https://www.mayoclinic.org/diseases-conditions/traumatic-brain-injury/symptoms-causes/syc-20378557>
- [3] Centers for Disease Control and Prevention. (n.d.). *National Center for Health Statistics Mortality Data on CDC WONDER*. Centers for Disease Control and Prevention. Retrieved March 1, 2023, from <https://wonder.cdc.gov/mcd.html>, https://www.cdc.gov/traumaticbraininjury/get_the_facts.html
- [4] Kucewicz, J. C., Dunmire, B., Leotta, D. F., Panagiotides, H., Paun, M., & Beach, K. W. (2007). Functional tissue pulsatility imaging of the brain during visual stimulation. *Ultrasound in Medicine & Biology*, 33(5), 681–690. <https://doi.org/10.1016/j.ultrasmedbio.2006.11.008>
- [5] Shah A, Irshad A. Sonography Doppler Flow Imaging Instrumentation. [Updated 2022 May 3]. In: StatPearls [Internet]. Treasure Island (FL): StatPearls Publishing; 2023 Jan-. Available from: <https://www.ncbi.nlm.nih.gov/books/NBK580539/>
- [6] *Military*. Terason. (2017, March 31). Retrieved October 20, 2022, from <https://www.terason.com/military/>
- [7] Kucewicz, J. C., Dunmire, B., Giardino, N. D., Leotta, D. F., Paun, M., Dager, S. R., & Beach, K. W. (2008). Tissue pulsatility imaging of cerebral vasoreactivity during hyperventilation. *Ultrasound in Medicine & Biology*, 34(8), 1200–1208. <https://doi.org/10.1016/j.ultrasmedbio.2008.01.001>
- [8] Phan, N. (2022). *Deep Learning Methods to Identify Human Cranium, Brain Ventricles, and Intracranial Hemorrhage Using Tissue Pulsatility Ultrasound Imaging* (thesis).
- [9] Kim, H., Kim, G.-dong, Yoon, B. C., Kim, K., Kim, B.-J., Choi, Y. H., Czosnyka, M., Oh, B.-M., & Kim, D.-J. (2014). Quantitative analysis of computed tomography images and early detection of cerebral edema for pediatric traumatic brain injury patients: Retrospective study. *BMC Medicine*, 12(1). <https://doi.org/10.1186/s12916-014-0186-2>

- [10] Yuh, E. L., Mukherjee, P., Lingsma, H. F., Yue, J. K., Ferguson, A. R., Gordon, W. A., Valadka, A. B., Schnyer, D. M., Okonkwo, D. O., Maas, A. I. R., & Manley, G. T. (2013). Magnetic Resonance Imaging improves 3-month outcome prediction in mild traumatic brain injury. *Annals of Neurology*, 73(2), 224–235. <https://doi.org/10.1002/ana.23783>
- [11] Guo, D., Wei, H., Zhao, P., Pan, Y., Yang, H.-Y., Wang, X., Bai, J., Cao, K., Song, Q., Xia, J., Gao, F., & Yin, Y. (2020). Simultaneous classification and segmentation of intracranial hemorrhage using a fully convolutional neural network. *2020 IEEE 17th International Symposium on Biomedical Imaging (ISBI)*. <https://doi.org/10.1109/isbi45749.2020.9098596>
- [12] Narayana, P. A., Coronado, I., Robinson, M., Sujit, S. J., Datta, S., Sun, X., Lublin, F. D., Wolinsky, J. S., & Gabr, R. E. (2018). Multimodal MRI segmentation of brain tissue and T2-hyperintense white matter lesions in multiple sclerosis using deep convolutional neural networks and a large Multi-center image database. *2018 9th Cairo International Biomedical Engineering Conference (CIBEC)*. <https://doi.org/10.1109/cibec.2018.8641800>
- [13] Ternifi, R., Cazals, X., Desmidt, A. L., Camus, V., Cottier, J. P., Patat, F., & Remenieras, J. P. (2012). Correlation between leukoaraiosis and natural brain tissue velocity: A pilot study using ultrasound and MRI. *2012 IEEE International Ultrasonics Symposium*. <https://doi.org/10.1109/ultsym.2012.0236>
- [14] Thomas, W. (2022). *Human Cranium, Brain Ventricle and Blood Detection Using Machine Learning on Ultrasound Data* (thesis).
- [15] *Epidural hematoma*. UCLA Health System. (n.d.). <https://www.uclahealth.org/medical-services/neurosurgery/conditions-treated/epidural-hematomas>
- [16] *Acute subdural hematoma*. UCLA Health System. (n.d.-a). <https://www.uclahealth.org/medical-services/neurosurgery/conditions-treated/acute-subdural-hematomas>
- [17] Dominguez, M. (2019, December). *Epidural Hematoma*. Epidural Hematoma - Neurology - Medbullets Step 2/3. <https://step2.medbullets.com/neurology/120299/epidural-hematoma>
- [18] *Intracranial hemorrhage - statpearls - NCBI bookshelf*. NIH. (n.d.). <https://www.ncbi.nlm.nih.gov/books/NBK470242/>

- [19] *Intraventricular hemorrhage (IVH)*. Intraventricular Hemorrhage (IVH) | Boston Children's Hospital. (n.d.). <https://www.childrenshospital.org/conditions/intraventricular-hemorrhage>
- [20] Abraham, M. K., & Chang, W.-T. W. (2016). Subarachnoid hemorrhage. *Emergency Medicine Clinics of North America*, 34(4), 901–916. <https://doi.org/10.1016/j.emc.2016.06.011>
- [21] *Intracerebral Hemorrhage: Video, anatomy & definition* | osmosis. Osmosis from Elsevier. (n.d.). https://www.osmosis.org/learn/Intracerebral_hemorrhage
- [22] J. Kucewicz, "Kucewicz."
- [23] NIH. (n.d.). T test - statpearls - NCBI bookshelf. <https://www.ncbi.nlm.nih.gov/books/NBK553048/>
- [24] Fuentes, E. (2007). *Statistical and Machine Learning Techniques Applied to Algorithm Selection for Solving Sparse Linear Systems*.
- [25] *Svmmodel*. Find classification error for support vector machine (SVM) classifier - MATLAB. (n.d.). <https://www.mathworks.com/help/stats/classreg.learning.classif.compactclassificationsvm.loss.html>